

RESEARCH

Open Access



Asrij/OCIAD1 depletion reduces inflammatory microglial activation and ameliorates A β pathology in an Alzheimer's disease mouse model

Prathamesh Dongre¹, Madhu Ramesh², Thimmaiah Govindaraju^{2*} and Maneesha S. Inamdar^{1,3*}

Abstract

Background Alzheimer's disease (AD) is a neurodegenerative disorder characterized by the accumulation of amyloid-beta (A β) plaques and neurofibrillary tangles, neuroinflammation, and glial activation. Asrij/OCIAD1 (Ovarian Carcinoma Immunoreactive Antigen Domain containing protein 1) is an AD-associated factor. Increased Asrij levels in the brains of AD patients and mouse models are linked to the severity of neurodegeneration. However, the contribution of Asrij to AD progression and whether reducing Asrij levels is sufficient to mitigate A β pathology in vivo is unclear.

Methods To explore the impact of Asrij on AD pathology, we deleted *asrij* in the APP/PS1 mouse model of AD and analyzed the effects on AD hallmarks. We used the Morris water maze and open field test to assess behavioral performance. Using immunohistochemistry and biochemical analyses, we evaluated A β plaque load, neuronal and synaptic damage, and gliosis. Further, we utilized confocal microscopy imaging, flow cytometry, and RNA sequencing analysis to comprehensively investigate changes in microglial responses to A β pathology upon Asrij depletion.

Results Asrij depletion ameliorates cognitive impairments, A β deposition, neuronal and synaptic damage, and reactive astrogliosis in the AD mouse. Notably, Asrij-deficient microglia exhibit reduced plaque-associated proliferation and decreased phagocytic activation. Transcriptomic analyses of AD microglia reveal upregulation of energy metabolism pathways and downregulation of innate immunity and inflammatory pathways upon Asrij depletion. Mechanistically, loss of Asrij increases mitochondrial activity and impedes the acquisition of a pro-inflammatory disease-associated microglia (DAM) state. Reduced levels of proinflammatory cytokines and decreased STAT3 and NF- κ B activation indicate protective changes in AD microglia. Taken together, our results suggest that increased Asrij levels reported in AD, may suppress microglial metabolic activity and promote inflammatory microglial activation, thereby exacerbating AD pathology.

Conclusions In summary, we show that Asrij depletion ameliorates A β pathology, neuronal and synaptic damage, gliosis, and improves behavioral performance in APP/PS1 mice. This supports that Asrij exacerbates the AD

*Correspondence:

Thimmaiah Govindaraju

tgraju@jncasr.ac.in

Maneesha S. Inamdar

inamdar@jncasr.ac.in

Full list of author information is available at the end of the article



© The Author(s) 2025. **Open Access** This article is licensed under a Creative Commons Attribution-NonCommercial-NoDerivatives 4.0 International License, which permits any non-commercial use, sharing, distribution and reproduction in any medium or format, as long as you give appropriate credit to the original author(s) and the source, provide a link to the Creative Commons licence, and indicate if you modified the licensed material. You do not have permission under this licence to share adapted material derived from this article or parts of it. The images or other third party material in this article are included in the article's Creative Commons licence, unless indicated otherwise in a credit line to the material. If material is not included in the article's Creative Commons licence and your intended use is not permitted by statutory regulation or exceeds the permitted use, you will need to obtain permission directly from the copyright holder. To view a copy of this licence, visit <http://creativecommons.org/licenses/by-nc-nd/4.0/>.

pathology. Mechanistically, *Asrij* is critical for the development of DAM and promotes neuroinflammatory signaling activation in microglia, thus restricting neuroprotective microglial responses. Hence, reducing *Asrij* in this context may help retard AD. Our work positions *Asrij* as a critical molecular regulator that links microglial dysfunction to AD pathogenesis.

Keywords Alzheimer's disease, Amyloid beta, *Asrij*/OCIAD1, Disease-associated microglia (DAM), Mitochondria, Inflammatory signaling, Neuroinflammation

Background

Alzheimer's disease (AD) is a chronic, age-related, neurodegenerative disorder and the most common form of dementia. The disease pathology is characterized by the accumulation of extracellular amyloid beta ($A\beta$) plaques, intracellular neurofibrillary tangles, reactive glia, and neuroinflammation. These pathologies culminate in synaptic loss and neuronal damage, ultimately resulting in learning and memory decline [1]. Despite extensive studies on the etiology of AD and its disease pathogenesis, effective treatment strategies are lacking, necessitating the exploration of novel therapeutic targets [2]. Genome-wide association studies (GWAS) have identified several genetic loci with variants that alter protein function or expression and are highly implicated in the risk of AD [3]. Elucidating the mechanisms by which altered expression of AD-associated factors influence the initiation and progression of disease pathology, may help identify new potential disease-modifying treatments.

Comparative analysis of proteomics and gene expression datasets from AD patients and AD mouse models identified OCIAD1 (Ovarian Carcinoma Immunoreactive Antigen Domain protein 1)/*Asrij* as a brain vulnerability factor associated with neurodegeneration [4]. In AD, *Asrij* is upregulated via glycogen synthase kinase 3 beta ($GSK3\beta$)/ β -catenin and p53 signaling and promotes mitochondria-mediated neuronal apoptosis as shown by in vitro experiments. AD patients and AD mouse models have increased *Asrij* levels that correlate with disease severity [4]. Moreover, in the AD brain, increased *Asrij* levels are observed near senile plaques in the afflicted brain regions, namely the hippocampus and cortex, and are associated with dystrophic neurites. This suggests a potential role for *Asrij* in promoting neurodegeneration in AD. Hence, we tested whether decreasing *Asrij* levels in vivo may mitigate AD phenotypes.

Asrij plays critical roles in mammalian blood cell homeostasis [5], stem cell maintenance and differentiation [6, 7], and hematopoietic aging [8]. *Asrij* acts as a scaffold protein on endosomes to regulate multiple cellular signaling pathways in *Drosophila* and mice [6, 9]. It interacts with mitochondrial electron transport chain (ETC) complexes and controls their

assembly and activity in human pluripotent stem cells and cell lines [7, 10]. Moreover, *Asrij* is essential for mounting immune responses by modulating myeloid cell proliferation and function [5, 11]. *Asrij* expression is abundant in the hematopoietic system and brain. In the mouse and human brain, *Asrij* is expressed predominantly by neurons and microglia with little expression in astrocytes and oligodendrocytes [12] (<https://www.proteinatlas.org/ENSG00000109180-OCIAD1/single+cell+type/brain>). Despite the early findings linking misexpression of *Asrij* to AD, whether increased *Asrij* is a mere consequence of the disease or actively influences disease progression is not known. This motivated us to investigate the in vivo role of *Asrij* in AD pathology.

Here, we show that constitutive depletion of *Asrij* in the APP/PS1 mouse model of AD boosts microglial metabolic activity and attenuates pro-inflammatory disease-associated microglia (DAM) responses. This possibly reduces $A\beta$ deposition, decreases neuronal and synaptic loss, curtails neuroinflammation, and improves cognition. Thus, *Asrij* is a crucial regulator of AD pathology.

Methods

Mice

Generation of the *asrij* floxed and knockout (KO) mice has been described previously [5]. B6.Cg-Tg(APP^{swe},PSEN1^{dE9})85Dbo/MmjaxAPP/PS1 (APP/PS1) mice (Stock #034832-JAX) and C57BL/6 J mice (Stock #000664-JAX) were purchased from the Jackson Laboratory. *asrij*^{-/-} mice were crossed to APP/PS1 mice to obtain heterozygous APP/PS1/*asrij*[±] mice. APP/PS1/*asrij*[±] mice were further crossed to *asrij*[±] mice to generate the experimental mice, APP/PS1⁻/*asrij*^{+/+} (denoted as wild type [WT]), APP/PS1⁻/*asrij*^{-/-} (denoted as KO), APP/PS1⁺/*asrij*^{+/+} (denoted as AD) and APP/PS1⁺/*asrij*^{-/-} (denoted as AD/KO). All mice were genotyped using polymerase chain reaction (PCR) before experiments. Mice of both sexes were randomly allocated to experimental groups unless otherwise noted. Mice were maintained at the Jawaharlal Nehru Centre for Advanced Scientific Research (JNCASR) animal facility under ambient temperature (23 ± 1.5 °C), 12 h light–dark

cycle and with ad libitum standard rodent chow diet and water. All mice experiments and protocols were approved by the JNCASR institutional animal ethics committee and were conducted in compliance with the guidelines and regulations.

Mouse behavioral tests

For all behavioral experiments, 10 month-old male mice were used. Prior to experiments, mice were handled for three consecutive days for acclimatization. Mice were transferred to the behavior test room 30 min before the onset of the test. Open field test (OFT) was used to assess the exploratory and anxiety-like behavior as described previously [13]. Briefly, each mouse was introduced into a 50 cm × 50 cm × 20 cm chamber and allowed to move freely for 5 min. 70% ethanol was used to clean the OFT apparatus between consecutive trials. The Morris water maze (MWM) test was used to evaluate learning and memory, as described previously [13]. Briefly, a circular water pool of 122 cm diameter and 90 cm depth was filled with water up to 60 cm, and the maze was virtually divided into four quadrants. A 14 cm² platform was placed submerged in one quadrant. Non-toxic white paint was added to the water to keep the tank opaque, and the pool temperature was maintained at 25 °C throughout the experiment. During the first 5 days of training (acquisition), each mouse was subjected to four trials per day with a different starting location for each trial. In each trial, the mouse was placed into the pool facing the wall and allowed 1 min to find the hidden platform. If unable to find the platform, the experimenter would guide the animal towards the platform and let it sit for 20 s before returning to the home cage, and the latency will be recorded as 60 s. On day 7, the escape platform was removed, and the swimming trajectories of the mice during the 60 s trial were recorded. For behavioral tests, mice activity was recorded using an overhead video camera (Sony, #SSC-G118) and analyzed using Smart v3.0 video tracking software (Panlab).

Immunohistochemistry

Mice were euthanized by cervical dislocation, and brains were swiftly isolated and bisected in ice-cold phosphate-buffered saline (PBS). The left hemisphere underwent fixation in 4% paraformaldehyde (PFA) for 48 h at 4 °C. Hippocampi and cortices were micro-dissected from the right hemisphere and flash frozen for storage at – 80 °C for subsequent protein and RNA extraction. Post fixation, hemibrains were transferred to 30% sucrose for cryoprotection and rehydration for 48 h at 4 °C until sunken in the solution. Samples were mounted and frozen in PolyFreeze tissue freezing medium (Sigma-Aldrich, #SHH0026). 30 μm coronal cryosections were obtained

using a cryostat (Leica, #CM3050S) and collected on 0.3% gelatin-coated glass slides, and slides were stored at – 80 °C until further use. For immunofluorescence staining, slides were thawed to room temperature (RT) and washed twice for 5 min with PBS + 0.05% sodium azide, followed by permeabilization with 0.3% Triton X-100 (Sigma-Aldrich, #T8787) in PBS for 1 h at RT. Sections were blocked in 4% fetal bovine serum (FBS) (Gibco, #10270106) for 1 h at RT and then incubated with primary antibodies diluted in blocking solution overnight at 4 °C. The following primary antibodies were used: Aβ (D54D2) (Cell Signaling Technology, #8243, 1:300), Aβ (6E10) (BioLegend, #803001, 1:200), LAMP1 (Abcam, #ab24170, 1:200), APP (Abcam, #ab32136, 1:200), GFAP (Invitrogen, #130300, 1:200), S100B (Cell Signaling Technology, #90393S, 1:100), IBA1 (Synaptic Systems, #234 009, 1:200), CD68 (Cell Signaling Technology, #97778S, 1:100), Ki67 (Cell Signaling Technology, #9129S, 1:50), CLEC7A (InvivoGen, #mabg-mdect, 1:50) and TMEM119 (Synaptic Systems, #400 002, 1:200). After primary antibody incubation, sections were washed thrice for 10 min with PBS + 0.05% Triton X-100 and then incubated with 1:400 diluted Alexa fluor 488, 568 or 633 conjugated anti-rabbit, -mouse, -rat and -chick secondary antibodies (Invitrogen) as appropriate, diluted in blocking solution for 1 h at RT. Sections were again washed thrice for 10 min with PBS + 0.05% Triton X-100. To visualize plaques, sections were stained with 1% Thioflavin S (ThioS) (Sigma-Aldrich, #T1892) solution in 50% ethanol for 8 min at RT, followed by three 2 min washes with 50% ethanol. After one PBS wash, sections were mounted in ProLong gold antifade mountant (Invitrogen, #P36930) containing 4',6-diamidino-2-phenylindole (DAPI) (Roche, #10236276001, 1:500) with coverslips.

Immunoblotting

Frozen hemibrains were thawed on ice and mechanically homogenized using tissue tearor (Biospec Products, #985370) in 500 μL western blot lysis buffer containing 20 mM 4-(2-hydroxyethyl)-1-piperazineethanesulfonic acid (HEPES) (pH=7.5), 150 mM NaCl, 5 mM MgCl₂, 5 mM ethylenediaminetetraacetic acid (EDTA) (pH=8), 0.5% Triton X-100, 10% glycerol, 5 mM dithiothreitol (DTT), 1 mM phenylmethylsulfonyl fluoride (PMSF), 10 mM NaF, 1 mM Na₃VO₄, 1X protease inhibitor cocktail (Sigma-Aldrich, #P8340) and 10 μM MG-132 (Sigma-Aldrich, #M7449) on ice. The homogenates were incubated on an end-to-end rotor for 4 h at 4 °C for lysis and then spun down at 16,000 rcf for 30 min at 4 °C. The supernatant was stored at – 80 °C, and total protein was estimated using Bradford assay (Bio-Rad, #5000006). For western blotting, equal amounts of

protein (40 μ g) were denatured in 1X Laemmli buffer containing 5% β -mercaptoethanol at 99 °C for 5–10 min. Samples were resolved on 10–12% sodium dodecyl sulfate (SDS) polyacrylamide gel at 150 V for 2 h using Mini-PROTEAN tetra cell (Bio-Rad, #1658004). Proteins were transferred on nitrocellulose membrane at 100 V for 2 h using the Mini trans-blot cell (Bio-Rad, #1703930). Membranes were blocked with 5% skim milk diluted in PBST (PBS+0.1% Tween 20) for 1 h at RT on a rocker. Following primary antibodies were diluted in PBST and used at 4 °C overnight: APP (Abcam, #ab32136, 1:1000), OCIAD1 (Abcam, #ab91574, 1:1000), GFAP (Cloud-Clone Corp., #PAA068Mu02, 1:1000), IBA1 (Cell Signaling Technology, #17198S, 1:1000), CD68 (Cell Signaling Technology, #97778S, 1:1000), PSD95 (Cell Signaling Technology, #3450S, 1:1000), Synaptophysin (Cell Signaling Technology, #36406S, 1:2000), STAT3 (Cell Signaling Technology, #9139S, 1:1000), Phospho-STAT3 (Tyr705) (Cell Signaling Technology, #9145S, 1:1000), NF- κ B p65 (Cell Signaling Technology, #8242S, 1:1000), Phospho-NF- κ B p65 (Ser536) (Cell Signaling Technology, #3033S, 1:1000), Akt (Cell Signaling Technology, #4691, 1:1000), Phospho-Akt (Ser243) (Cell Signaling Technology, #4060, 1:1000), mTOR (Abcam, #ab2732, 1:1000), Phospho-mTOR (Ser2448) (Abcam, #ab109268, 1:1000), GAPDH (Sigma-Aldrich, #G9545, 1:4000) and α -tubulin (Sigma-Aldrich, #T8203, 1:2000). Blots were washed thrice for 5 min in PBST and then probed with 1:2000 diluted horseradish peroxidase (HRP)-conjugated anti-rabbit and anti-mouse secondary antibodies (GeNei) for 1 h at RT. After three 5 min washes, blots were developed on X-ray films using Clarity western enhanced chemiluminescence (ECL) reagent (Bio-Rad, #1705061). Band intensities were quantified using Fiji.

Isolation of microglia from mouse brain

Whole brains isolated from 10 month-old mice were immediately minced into small pieces with a sterile surgical blade in ice-cold Hanks' balanced salt solution (HBSS) (Thermo Fisher Scientific, #14175095). Tissue chunks were dissociated by mechanical homogenization in 10 mL 1X HBSS containing 15 mM EDTA, 1.5 mM HEPES, and 0.5% glucose by 6–8 gentle strokes in a glass Dounce homogenizer. Homogenates were filtered through 70 μ m cell strainers to obtain single-cell suspensions and spun down at 170 rcf for 10 min at 4 °C. Myelin removal was done using Percoll density gradient centrifugation. Briefly, 100% Percoll solution was prepared by mixing absolute Percoll (GE Healthcare, #GE17-0891-02) in 10X Dulbecco's PBS (DPBS) (Thermo Fischer Scientific, #14080055) at a 9:1 ratio and further diluted to 37% using 1X DPBS. Cell pellets

were resuspended in 37% isotonic Percoll followed by centrifugation at 600 rcf for 15 min at 4 °C with minimum acceleration and no brake. The supernatant and myelin layer were aspirated and discarded, and the pellets were washed once with DPBS. Microglia were isolated using Magnetic-activated cell sorting (MACS). Briefly, cells were resuspended in 100 μ L MACS buffer (PBS (pH 7.2)+0.5% bovine serum albumin (BSA)+2 mM EDTA+0.05% sodium azide) and incubated with 25 μ L CD11b (Microglia) microbeads (Miltenyi Biotec, #130-093-634) on ice for 30 min. Labeled cell suspensions were passed through pre-rinsed LS columns (Miltenyi Biotec, #130-042-401) on a MidiMACS separator magnet (Miltenyi Biotec, #130-042-302), and columns were washed with 5 mL MACS buffer. After removing the columns from the magnet, column-bound cells were plunged with 3 mL MACS buffer and used as purified CD11b⁺ microglia. 4–4.5 \times 10⁵ microglia were obtained per mouse with ~90% cell viability.

Flow cytometry

Dissociated cells obtained after Percoll density gradient centrifugation were resuspended in 100 μ L FACS buffer (PBS (pH 7.2), 1% BSA+1 mM EDTA+0.05% sodium azide) and incubated with CD45-APC-Cy7 (BioLegend, #103116) and CD11b-FITC (BioLegend, #101205) antibodies at 1:100 dilution on ice for 1 h. Cells were washed with FACS buffer at 3000 rcf for 3 min. For analysis of mitochondrial parameters, cells were stained with 25 nM Mitotracker Deep Red (Invitrogen, #M22426) or 50 nM Tetramethylrhodamine, Methyl Ester, Perchlorate (TMRM) (Invitrogen, #T668), or 5 μ M MitoSOX Red (Invitrogen, #M36007) diluted in PBS at 37 °C for 30 min. Cells were washed with FACS buffer, stained with 7-Amino-actinomycin D (7-AAD) (BD Biosciences, #559925) at 1:500 dilution for 10 min at 37 °C and analyzed using a BD FACSaria Fusion flow cytometer (BD Biosciences). Debris was excluded using forward and side-scatter pulse area parameters (FSC-A and SSC-A), followed by singlet gating using forward and side-scatter pulse width parameters (FSC-H and SSC-W). Further, 7-AAD⁻ population which consists of live cells was used to gate microglia. Microglia were gated as CD11b⁺ CD45^{int} and median fluorescence intensity (MFI) was quantified. All analysis was carried out using FlowJo v10 software (BD Biosciences).

In vitro A β phagocytosis assay

To prepare A β oligomers, 1 mg lyophilized A β ₁₋₄₂, HiLyte™ Fluor 555-labeled peptide (AnaSpec, #AS-60480-01) was reconstituted in 1% ammonia solution (NH₄OH) and then diluted to prepare 100 μ M stock solution. 100 μ M of monomeric A β was incubated for

24 h at 4 °C in Ham's F12 media (Gibco, #11765054) to make a 50 μ M stock of oligomeric A β as published previously [14, 15]. For A β uptake assay, microglia were incubated with 5 μ M oligomeric HiLyte™ Fluor 555 labeled A β in Iscove's modified Dulbecco's medium (IMDM) (Gibco, #12440053) supplemented with 10% FBS for 1 h at 37 °C. Cells were washed once with PBS and spun down at 3000 rcf for 3 min at 4 °C. Following staining with CD11b-FITC and CD45-APC-Cy7 antibodies, samples were analyzed using a BD FACSAria Fusion Flow Cytometer (BD Biosciences).

Confocal imaging and analysis

Tile scan images of whole brain sections were captured using CQ1 confocal image cytometer (Yokogawa Electric) at 20X magnification. Dentate gyrus region of the hippocampus and somatosensory region of the cortex were imaged on a Zeiss laser scanning confocal microscope (LSM) 880 (Zeiss) using 20X and 63X objectives with a *z*-interval of 0.5 μ m. To measure plaque density and percent staining area, 20X images from 3 serial sections per mouse were analyzed. Using Fiji, the images were exported to 8-bit format following background subtraction (rolling-ball radius, 50 pixels) and percent staining area was recorded after thresholding. Cell count analysis for 20X images was performed using the 'analyze particles' function in Fiji. For analysis requiring high magnification images, a 63X oil-immersion objective was used with 1X or 2X optical zoom and a *z*-interval of 0.5 μ m. A minimum of 10–15 individual plaques per brain section were imaged with 3 sections per mouse. To measure plaque-associated microglia, IBA1 staining was thresholded and converted to binary mask. DAPI⁺ nuclei that overlap with IBA1⁺ mask were manually counted. To measure microglial A β engulfment and plaque volume, 3D surface renderings were created for IBA1, CD68, and ThioS using the 'surface' module of Imaris 9.5 software (Bitplane). CD68 and ThioS overlapping surfaces were visualized in a separate channel, and volume was recorded. Microglial skeleton analysis was performed using the 'filament' module in Imaris. A minimum of 10–15 individual cells per brain section were analyzed with 3 sections per mouse. Maximum intensity projections are shown for all representative images.

Enzyme-linked immunosorbent assay (ELISA)

For soluble A β _{1–42} quantification, supernatants (soluble fractions) collected after homogenization of cortices were used. To extract protein for insoluble A β _{1–42} estimation, pellets underwent guanidine extraction. Briefly, brain homogenate pellets were incubated with 5 M Guanidine HCl/50 mM Tris (pH=8.0) in a 1:6 ratio at RT for 3 h.

Samples were diluted 1:5 in PBS containing 1X protease inhibitor cocktail and centrifuged at 16,000 rcf for 20 min at 4 °C. The supernatant (insoluble fraction) was stored at – 80 °C until analysis. Protein concentrations of the fractions were determined using Bradford assay. Soluble and insoluble fractions were diluted 1:25 for ELISA. Human A β _{1–42} Quantikine ELISA kit (R&D Systems, #DAB142) was used for standard curve generation, and the assay was performed as per the manufacturer's instructions. To measure cytokine levels in the brain, BD OptEIA mouse IL-6 (BD Biosciences, #550950), BD OptEIA TNF- α (BD Biosciences, #560478) and mouse IL-1 β (ABclonal, #RK00006) ELISA kits were used as per manufacturer's instructions. Absorbance was measured using Varioskan LUX multimode microplate reader (Thermo Fischer Scientific).

RNA isolation and reverse transcription-quantitative PCR (RT-qPCR)

To isolate RNA, the MACS-sorted CD11b⁺ microglia were resuspended in 500 μ L ice-cold TRIzol reagent (Invitrogen, #15596026) and lysed by vortexing. After incubation at RT for 5 min, 100 μ L chloroform was added and mixed by gently inverting the tubes. Samples were spun down at 16,000 rcf for 10 min at 4 °C. The upper aqueous phase was collected and incubated with an equal volume of 100% isopropanol overnight at – 20 °C to precipitate RNA. Samples were centrifuged at 16,000 rcf for 20 min at 4 °C and the RNA pellet was washed once with 70% ethanol. The pellet was allowed to air dry for 5–10 min at RT and then dissolved in 25 μ L ultrapure nuclease-free water (Thermo Fischer Scientific, #10977015). RNA quantity and quality were assessed using a NanoDrop 2000 Spectrophotometer (Thermo Fischer Scientific). cDNA was synthesized using 200–400 ng total RNA in SuperScript III first-strand synthesis kit (Invitrogen, #18080051) following the manufacturer's instructions. RT-qPCR was set up using SensiFAST SYBR No-ROX kit (Bioline, #BIO-98020) in CFX384 real-time PCR system (Bio-Rad) as per the manufacturer's protocol. Following primers were used: *asrij* forward 5'-GGAGATCTCGAGATGAATGGGAGGGCTGATTTT-3' and reverse 5'-GTGGTGGCGGCCGCTCACTCA TCCCAAGTATCTCC-3'; β -*actin* forward 5'-GTGACG TTGACATCCGT-3' and reverse 5'-GCCGGACTCATC GTACTCC-3'. All reactions were set up in duplicates, and β -*actin* was used as the loading control.

RNA sequencing and analysis

RNA isolated from 4–4.5 $\times 10^5$ MACS-sorted microglia by the TRIzol method was quantified using Qubit RNA high-sensitivity assay kit (Invitrogen, #Q32852) on Qubit 4 fluorimeter (Invitrogen). Samples were run on the

tapeStation system (Agilent) utilizing high sensitivity RNA ScreenTape analysis (Agilent, #5067-5579) for RNA quality control (QC). Sample QC, library preparation, and RNA sequencing were done by the next generation genomics facility at the Bangalore Life Science Cluster (BLiSC), India. Briefly, ribosomal RNA (rRNA) depletion was performed using NEBNext rRNA depletion kit v2 (Human/Mouse/Rat) with RNA sample purification beads (NEB, #E7405X). cDNA libraries were constructed utilizing the NEBNext Ultra II Directional RNA Library Prep (stranded) kit with sample purification beads (NEB, #E7765L). cDNA libraries were sequenced on the NovaSeq 6000 platform (Illumina) with 2×100 bp sequencing read length and ~100 million read depth per sample. Sequenced reads in FASTQ files were trimmed and filtered to remove adaptor sequences and low-quality bases, respectively, using the fastp tool [16] (<https://github.com/OpenGene/fastp>). Data quality was checked using the FastQC tool (<https://github.com/s-andrews/FastQC>). Reads were aligned to the indexed UCSC mm10 mouse reference genome using HISAT 2 [17] (<https://github.com/DaehwanKimLab/hisat2>). SAM files were converted and sorted/indexed by coordinate to BAM files using Samtools [18] (<https://github.com/samtools/samtools>). FeatureCounts program of the Subread R package was used to calculate and summarize per-gene read counts as expression values [19] (<https://rnh.github.io/bioinfo-notebook/docs/featureCounts.html>). DESeq2 (v1.30.0) was utilized for differential gene expression (DEG) analysis [20] (<https://www.bioconductor.org/packages/release/bioc/vignettes/DESeq2/inst/doc/DESeq2.html>). Principal component analysis (PCA) plots were generated using the plotPCA command in DESeq2. DEGs ($p < 0.01$) with \log_2 fold change > 1.0 were considered upregulated, and \log_2 fold change < -1.0 were considered downregulated. Volcano plots were generated using the ggplot2 package (<https://ggplot2.tidyverse.org/>). Heatmaps were visualized using the pheatmap R package (<https://github.com/raivokolde/pheatmap>). Gene ontology (GO) and pathway enrichment analysis was conducted using the Enrichr web tool [21] (<https://maayanlab.cloud/Enrichr/>) and MSigDB collection.

GO terms and pathways with False Discovery Rate (FDR) < 0.05 were considered statistically significant.

Statistical analysis

Each data point in the graphs represents an individual mouse. All data are presented as mean \pm standard error of mean (SEM). Statistical significance between the two groups was determined using a two-tailed unpaired Student's *t*-test. Comparisons between more than two groups were made using one-way, two-way, or repeated measures analysis of variance (ANOVA) with Bonferroni's or Tukey's multiple comparisons post-hoc test. All statistical analyses and graph plotting were performed in Prism 10 software (GraphPad). *P* values less than 0.05 were considered significant. *P* values less than 0.01 were considered significant for differential gene expression analysis of RNA sequencing data. For gene ontology and pathway enrichment analysis, terms with false discovery rate (FDR) < 0.05 were analysed, ns: not significant, * $P < 0.05$, ** $P < 0.01$, and *** $P < 0.001$.

Results

Asrij depletion alleviates cognitive deficits and anxiety-like behavior in APP/PS1 mice

To investigate how Asrij impacts A β pathology and Alzheimer's disease (AD)-related behavior, we crossed *asrij*^{-/-} (knockout [KO]) mice with *APP/PS1* mice, a well-studied mouse model of AD, to generate *APP/PS1*⁺*asrij*^{-/-} (referred to as AD/KO) mice. We used *APP/PS1*⁻*asrij*^{+/+} (referred to as wild type [WT]) mice, *APP/PS1*⁻*asrij*^{-/-} (referred to as KO) mice, and *APP/PS1*⁺*asrij*^{+/+} (referred to as AD) mice as controls (Fig. S1A–B). Immunoblotting analysis confirmed that Asrij levels were increased in AD mice and were undetectable in AD/KO mice (Fig. S1C).

APP/PS1 mice exhibit learning and memory deficits from 9 months of age [22]. To evaluate the effect of Asrij depletion on cognitive performance, we performed the Morris water maze (MWM) test using 10 month-old mice (Fig. 1A). Over the first 5 days

(See figure on next page.)

Fig. 1 Asrij depletion alleviates cognitive deficits and anxiety-like behavior in APP/PS1 mice. **A** Schematic showing behavioral tests used to assess cognitive performance of mice. **B** Graph shows quantification of latency to platform across 5 days of invisible platform training (acquisition) in Morris water maze (MWM) test ($n = 13$, all males) **C** Representative images of mouse tracks during MWM probe trial. The red circle indicates the location of the platform during training. Graphs show quantification of **D** latency, **E** cross number, **F** the percentage of time spent in the target quadrant, and **G** swimming speed (cm/s) during the MWM probe trial ($n = 13$, all males). **H** Representative traces of mouse path in open field test (OFT). The red box shows the center zone. Graphs show quantification of **I** entries in the center zone, **J** the percentage of distance traveled in the center zone, **K** the percentage of time spent in the center zone, **L** total distance traveled, and **M** mean speed (cm/s) in OFT ($n = 8$, all males). Statistical significance between experimental groups was calculated by repeated-measures two-way ANOVA with Bonferroni's post hoc test (**B**) and one-way ANOVA with Bonferroni's post hoc test (**D–G** and **I–M**). Error bars denote the mean \pm SEM. ns: non-significant, * $P < 0.05$, ** $P < 0.01$, and *** $P < 0.001$

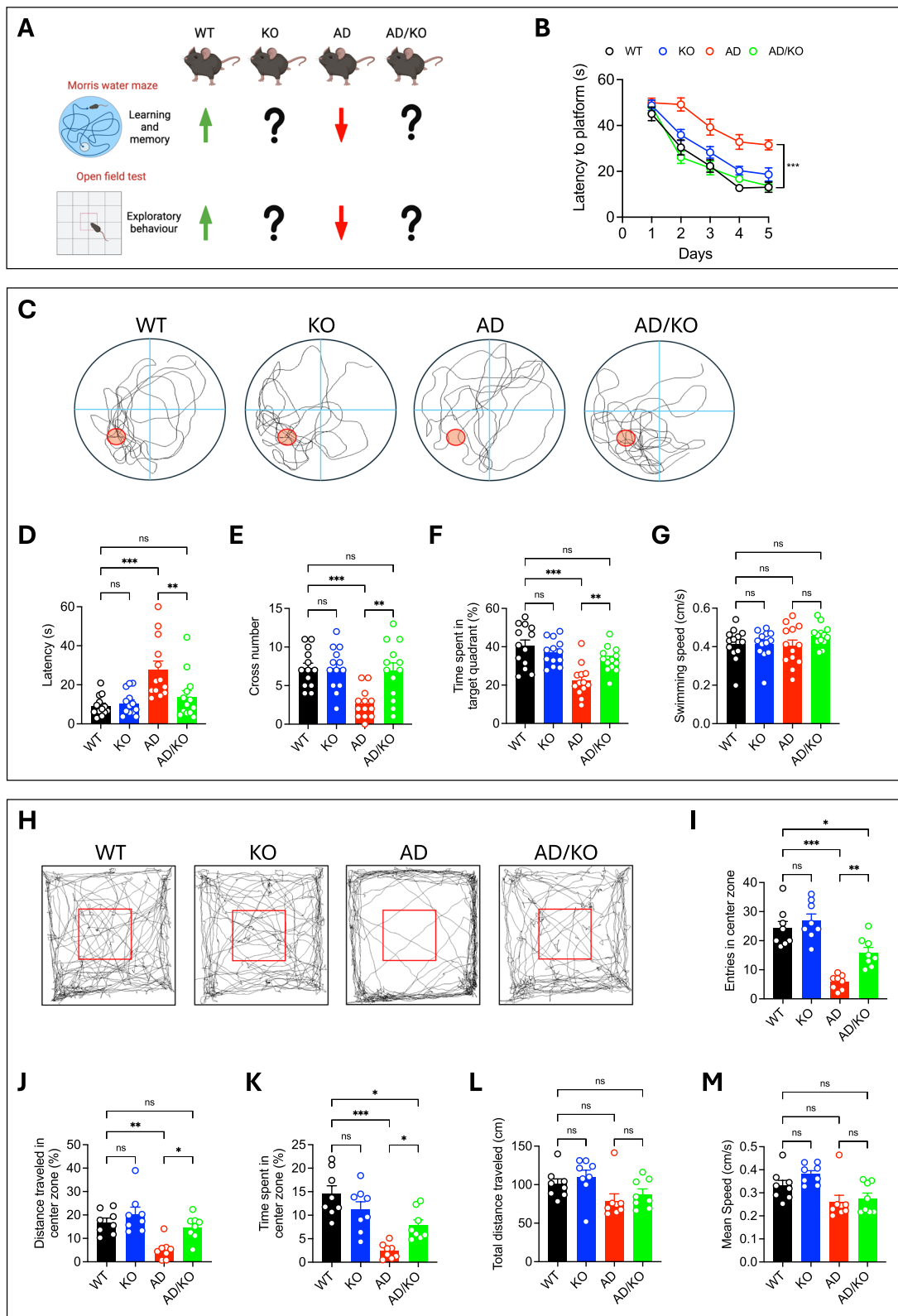


Fig. 1 (See legend on previous page.)

of the training phase, WT and KO mice showed gradually decreasing latency to find the submerged platform, which indicates intact spatial learning. AD mice took a substantially longer time searching for the hidden platform. Interestingly, AD/KO mice showed significantly reduced latency to find the platform as compared to AD mice, suggesting improved spatial learning abilities (Fig. 1B). The swimming path used by the mice to search for the hidden platform during the memory recall session on day 7 also reflects the extent of cognitive dysfunction. As seen from mouse path traces, AD mice adopted a random and non-directed navigation path, but AD/KO mice performed a focused and self-orienting search for the platform. (Fig. 1C). Moreover, AD/KO mice showed reduced latency to the platform, increased crossing number, and spent significantly more time in the target quadrant, demonstrating restored spatial memory (Fig. 1D–F). Importantly, differences in performance in the MWM test did not arise due to defects in locomotor activity as comparable swimming speeds were noted for all the genotypes (Fig. 1G). We did not find any appreciable difference in MWM test parameters between WT and KO mice suggesting that *Asrij* depletion does not affect learning and memory, in the absence of A β pathology. Thus, *Asrij* deficiency alleviates learning and memory defects in *APP/PS1* mice.

A β pathology is also known to reduce exploratory behavior and spur anxiety-like behavior in *APP/PS1* mice, wherein they tend to spend more time in the periphery of an open field, referred to as thigmotaxis, a measure of anxiety [22]. Therefore, we evaluated the effect of *Asrij* depletion on these behaviors using the open field test (OFT). During the 5 min free exploration period, AD mice had reduced entries in the center, spent less time, and covered less distance in the center zone of an open field compared to WT mice, suggesting elevated anxiety. Interestingly, AD/KO mice showed increased center entries and increased time spent and distance covered in the center (Fig. 1H–K). *Asrij* depletion in the absence of A β pathology did not affect performance in the OFT as there was a comparable level of exploratory behavior between WT and KO mice. Further, no differences were recorded in the total distance traveled and speed of mice of all four genotypes, suggesting that results obtained in OFT were not due to altered locomotor activity (Fig. 1L–M). Thus, *Asrij* depletion improves exploratory behavior and limits anxiety-like phenotypes in *APP/PS1* mice. Taken together, our results suggest that an increase in *Asrij* levels in AD potentially precipitates neurobehavioral and cognitive dysfunction in AD.

***Asrij* depletion reduces A β plaque deposition and associated pathology in *APP/PS1* mice**

In the *APP/PS1* mice, A β plaque deposition and neuroinflammation begins at around 4 months and progresses gradually, resulting in a full-blown disease by 10 months of age [23]. To determine whether *Asrij* influences the accumulation of A β plaques, we first stained brain cryosections with Thioflavin S (ThioS), which marks the dense core compact A β plaques. We did not observe a significant difference in plaque load between 5 month-old AD and AD/KO mice (Fig. S2A). However, 10 month-old AD/KO mice exhibited a remarkable reduction in A β plaques in the cortex and hippocampus compared to AD mice (Fig. 2A). In parallel, we also assessed the accumulation of total A β in the brain using the D54D2 antibody, which recognizes the total A β peptide burden including various isoforms such as the most abundant A β ₄₀ (relatively inert) and A β ₄₂ (highly neurotoxic) species. Immunostaining analysis revealed significantly reduced total A β levels in the cortex and hippocampus of AD/KO mice (Fig. 2B). This indicates that *Asrij* depletion limits A β plaque accumulation in *APP/PS1* mice.

Soluble A β oligomers, which are highly neurotoxic, aggregate to form insoluble fibrils and, subsequently, compact plaques [24]. To evaluate whether the absence of *Asrij* alters the soluble and insoluble forms of A β in AD mice, we quantified the concentration of A β ₄₂ species in the soluble (phosphate buffered saline (PBS)-extracted) and insoluble (guanidine hydrochloride-extracted) brain fractions using the enzyme-linked immunosorbent assay (ELISA). In alignment with the reduced A β staining observed in imaging studies, we detected substantially reduced amounts of A β ₄₂ in soluble and insoluble brain fractions (Fig. 2C). Notably, the levels of the full-length amyloid precursor protein (APP) and its cleaved carboxy-terminal fragments (CTF), CTF- α and CTF- β were unchanged, suggesting that reduction in plaques upon *Asrij* depletion does not result from altered APP processing (Fig. S2B). Altogether, these studies strongly support the idea that *Asrij* promotes A β plaque accumulation and that its absence reduces the overall A β burden in *APP/PS1* mice.

One of the major pathological features of AD is the presence of hypertrophic reactive glial fibrillary acidic protein (GFAP) positive astrocytes around A β plaques, that are known to propagate neurotoxicity [25]. To visualize reactive astrogliosis, we performed immunofluorescence staining for GFAP, an astrocyte marker whose levels increase upon activation, and S100 calcium-binding protein B (S100B), a pan-astrocyte marker. Note that cortical astrocytes do not express GFAP under homeostatic conditions, but in

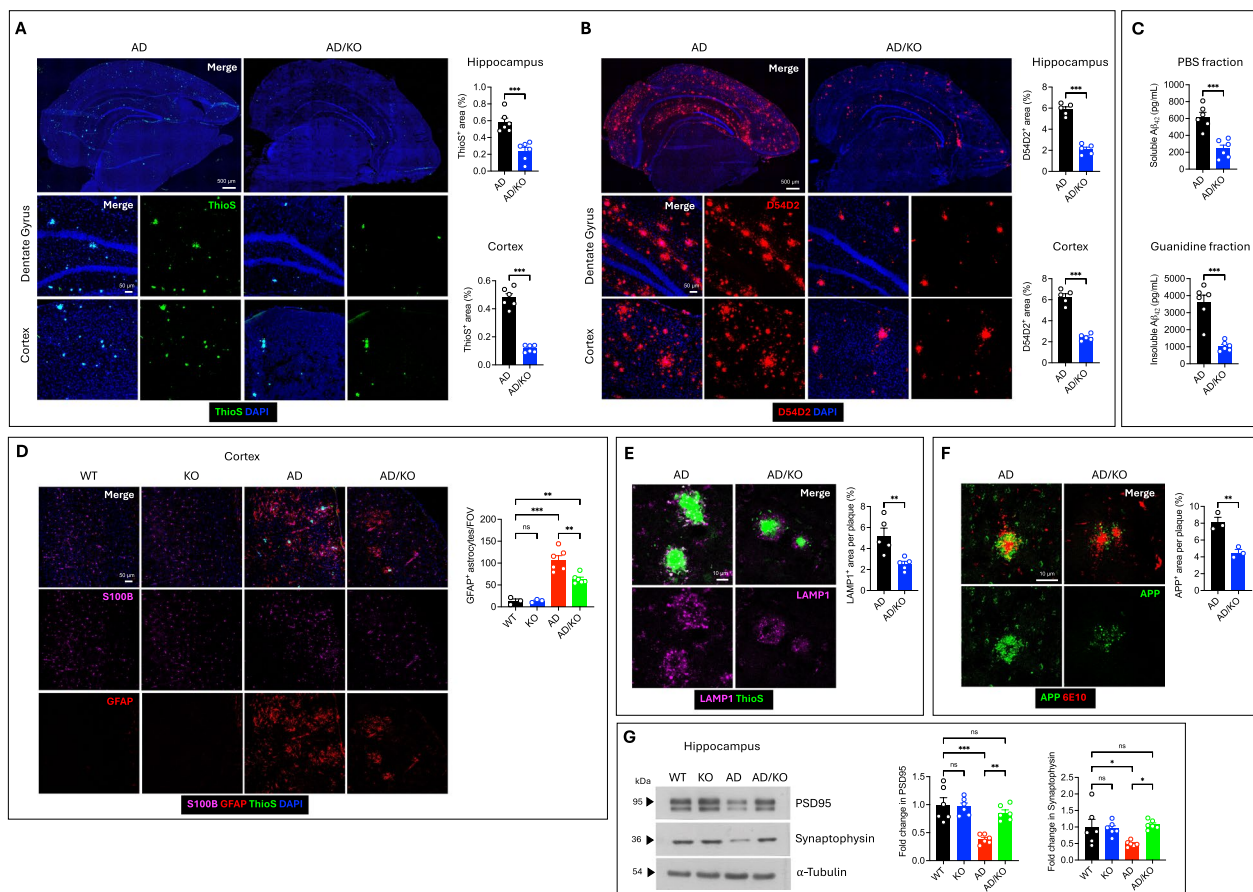


Fig. 2 Asrij depletion reduces A β plaque deposition and associated pathology in APP/PS1 mice. **A** Representative confocal images of brain sections showing Thioflavin S (ThioS) staining (green) for plaques. DAPI (blue) marks the nuclei. Graphs show quantification of percent area covered by ThioS⁺ staining in hippocampus and cortex (n = 6, all males). **B** Representative confocal images of brain sections showing A β staining (red) using D54D2 antibody. DAPI (blue) marks the nuclei. Graphs show quantification of percent area covered by A β staining in hippocampus and cortex (n = 5, all males). **C** Graphs show quantification of A β ₄₂ levels (pg/mL) in the soluble (PBS) and insoluble (guanidine) brain fractions by ELISA (n = 6, all males). **D** Representative confocal images showing S100B (magenta) and GFAP (red) staining for astrocytes in the cortex. ThioS (green) and DAPI (blue) mark plaques and nuclei, respectively. Graph shows quantification of GFAP⁺ astrocytes per field of view (FOV) of the cortex averaged over 4 FOVs per section with 3 sections per mouse (n = 3 for WT and KO, n = 6 for AD and AD/KO, all males). **E** Representative confocal images showing LAMP1 staining (magenta) around ThioS⁺ A β plaques (green). Graph shows quantification of LAMP1⁺ area per plaque averaged over 15 plaques per section with 3 sections per mouse (n = 5, all males). **F** Representative confocal images showing APP staining (green) around 6E10⁺ A β plaques (red). Graph shows quantification of APP⁺ area per plaque averaged over 15 plaques per section with 3 sections per mouse (n = 3, all males). **G** Immunoblot analysis of PSD95 and Synaptophysin levels in the hippocampus. α -tubulin is loading control. Graphs show fold change in PSD95 and Synaptophysin levels normalized to α -tubulin (n = 6, all males). Statistical significance between experimental groups was calculated by unpaired two-tailed Student's t-test (**A-C** and **E-F**) and one-way ANOVA with Tukey's post hoc test (**D** and **G**). Error bars denote mean \pm SEM. ns: non-significant, * P < 0.05, ** P < 0.01, and *** P < 0.001

conditions of disease or injury, GFAP immunoreactivity in the cortex represents astrocyte activation [25]. Indeed, we found a marked increase in the number of GFAP⁺ astrocytes in the cortex of AD mice. AD/KO mice showed reduced GFAP⁺ astrocytes in the cortex as compared to AD mice (Fig. 2D). Consistently, immunoblotting analyses showed reduced GFAP protein levels (Fig. S2C). Thus, Asrij depletion attenuates A β associated astrocyte activation, in line with the reduced neuropathology.

Extracellular A β deposits are surrounded by swollen dystrophic axons and dendrites of neurons, called dystrophic neurites, that are marked by abnormal accumulation of lysosomal-associated membrane protein 1 (LAMP1) and APP [26]. Given the improved behavioral performance and reduced A β deposition in AD/KO mice, we next quantified LAMP1 and APP immunoreactivity. We found that plaques in AD/KO mice were covered by reduced LAMP1 and APP staining, suggesting attenuated neuronal dystrophy (Fig. 2E, F). Additionally, the absence

of *Asrij* restored levels of post-synaptic marker, post synaptic density 95 (PSD95) and pre-synaptic marker, Synaptophysin, indicating synaptic protection (Fig. 2G). Collectively, these results show that *Asrij* depletion prevents A β induced neuronal and synaptic damage.

Reduced microgliosis and microglial A β phagocytosis in *Asrij* deficient *APP/PS1* mice

Microglia are brain-resident innate immune cells that play beneficial and detrimental roles in a context-specific manner in AD [27]. In response to A β , microglia undergo activation, wherein they are recruited to the plaques, undergo local proliferation, and form a physical barrier to protect neurons from A β -mediated toxicity [28]. Microglial A β phagocytosis contributes to A β clearance [29] but also promotes the formation and deposition of A β plaques [30–32]. Interestingly, publicly available datasets revealed marginally increased *Asrij* expression in AD microglia (Fig. S3A–B). We also performed reverse transcriptase-quantitative polymerase chain reaction (RT-qPCR) and immunoblotting analyses for *Asrij* on magnetic-activated cell sorting (MACS)-sorted CD11b⁺ mouse microglia. Consistently, AD microglia had increased transcript and protein levels of *Asrij*, compared to WT microglia (Fig. S3C–D). This hints that *Asrij* may be necessary in regulating microglial responses to A β pathology. Additionally, *Asrij* controls myeloid cell function and immune responses in *Drosophila* and mice [5, 11]. Increased *Asrij* levels in AD microglia, combined with reduced A β pathology, led us to hypothesize that *Asrij* may alter microglial activity in AD mice.

To evaluate microgliosis and phagocytic activation, we performed immunofluorescence staining for a microglial marker, ionized calcium-binding adapter molecule 1 (IBA1), and a phagolysosomal marker, cluster of differentiation 68 (CD68). AD/KO mice had fewer microglia in the hippocampus and cortex than AD mice. Further, CD68 coverage was significantly reduced in AD/KO mice, confirming lower microglial phagocytic activation (Fig. 3A, B). In agreement with our imaging results, immunoblotting analysis showed that IBA1 and CD68 levels were reduced in AD/KO mice (Fig. S4A). Low levels of microgliosis and phagocytic activation upon *Asrij* depletion appears to be specific to A β pathology as there was no significant difference in microglial numbers between WT and KO mice. We also observed reduced microglial clustering to A β plaques as seen by a two-fold reduction in the number of plaque-associated microglia in AD/KO as compared to AD mice (Fig. 3C). Proliferation is known to contribute to localized increase in microglial numbers around plaques [28]. Ki67 staining for assessing proliferation showed that AD/KO mice had fewer Ki67⁺ IBA1⁺ plaque-proximal microglia than

AD mice, indicating attenuated microglial proliferation (Fig. 3D). Thus, *Asrij* depletion results in reduced A β load and a consequent reduction of microglial proliferation. Hence, *Asrij* may be important for A β -driven microglial recruitment, proliferation and association with plaques.

Microglial A β phagocytosis shapes the extent of plaque accumulation and is a critical response to AD pathology [33]. To evaluate A β engulfment by microglia, we utilized Imaris-based 3D rendering of ThioS, IBA1, and CD68 staining. *Asrij* depleted microglia showed a three-fold reduction in the volume of ThioS⁺ plaques internalized within CD68⁺ phagosomes. Also, plaque-associated CD68 staining was lower in AD/KO mice indicating reduced microglial A β engulfment (Fig. 3E). As a secondary approach to assess microglial phagocytosis, we performed flow cytometry-based *in vitro* oligomeric A β uptake assay. The frequency of CD11b⁺ CD45^{int} microglia in AD/KO mice was lower than in AD mice, confirming reduced microgliosis observed in imaging studies (Fig. S4B–C). Also, levels of CD45 and CD11b, which are generic markers of activation, were significantly diminished in AD/KO mice (Fig. S4C). We did not observe any difference in microglial frequency and activation between WT and KO mice. Thus, *Asrij* depletion limits microgliosis and microglial activation in the context of A β pathology. When assessing A β uptake, approximately 40% of CD11b⁺ CD45^{int} microglia in WT and KO mice were positive for HiLyte Fluor 555 labeled oligomeric A β ₄₂, reflecting unchanged basal phagocytosis activity. As expected, AD microglia showed increased A β ₄₂ uptake while AD/KO microglia exhibited dampened A β phagocytosis with about 38% microglia ingesting labeled oligomers (Fig. S4D). These results provide evidence that *Asrij* critically contributes to the uptake and phagocytosis of A β plaques by microglia, in the AD mouse model.

Asrij deficiency upregulates metabolic genes and increases mitochondrial activity in AD microglia

To gain a comprehensive and unbiased assessment of molecular mechanisms by which *Asrij* impacts microglial homeostasis in AD, we performed bulk RNA sequencing (RNA-seq) on immunomagnetic bead-sorted CD11b⁺ microglia, isolated from the brains of AD and AD/KO mice (Fig. 4A). We found 651 upregulated genes (log₂ fold change > 1) and 257 downregulated genes (log₂ fold change < - 1) in AD/KO microglia compared to AD microglia (Fig. 4B and Fig. S5A). Gene ontology (GO) analysis of differentially expressed genes (DEGs) revealed upregulation of biological processes such as neuropeptide signalling, translation, mitochondrial ATP synthesis and NADH dehydrogenase activity among others (Fig. 4C). On

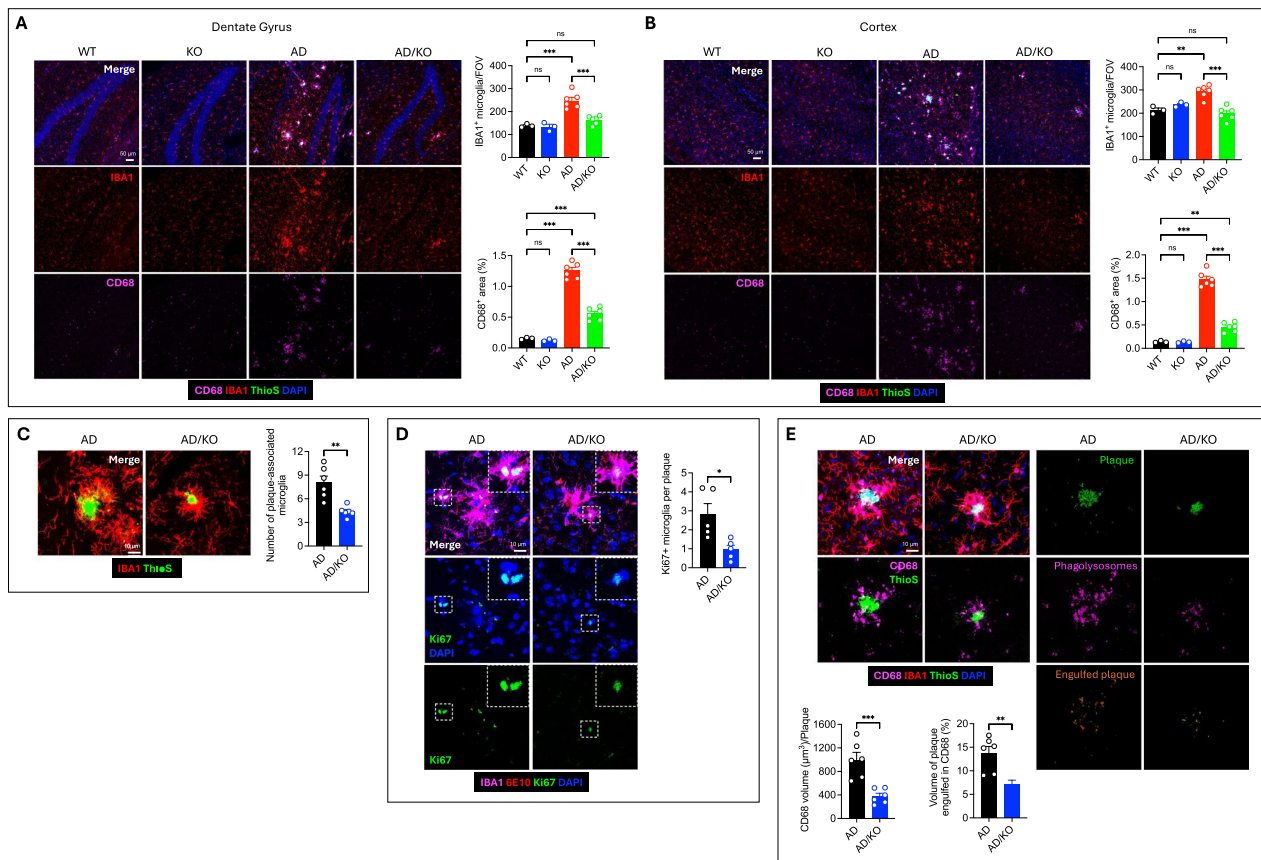


Fig. 3 Reduced microglial and microglial A β phagocytosis in Asrij deficient APP/PS1 mice. **A** Representative confocal images showing IBA1⁺ microglia (red), CD68⁺ phagolysosomes (magenta) and ThioS⁺ A β plaques (green) in the hippocampus. DAPI (blue) marks the nuclei. Graphs show quantification of microglial numbers and percent area covered by CD68 staining in the hippocampus per field of view (FOV) averaged over 3 FOVs per section with 3 sections per mouse (n = 3 for WT and KO, n = 6 for AD and AD/KO, all males). **B** Representative confocal images showing IBA1⁺ microglia (red), CD68⁺ phagolysosomes (magenta), and ThioS⁺ A β plaques (green) in the cortex. DAPI (blue) marks the nuclei. Graphs show quantification of microglial numbers and percent area covered by CD68 staining per FOV averaged over 3 FOVs per section with 3 sections per mouse (n = 3 for WT and KO, n = 6 for AD and AD/KO, all males). **C** Representative confocal images showing IBA1⁺ microglia (red) around ThioS⁺ A β plaque (green). Graph shows quantification of the number of microglia within a 15 μ m radius surrounding A β plaque averaged over 15 plaques per section with 3 sections per mouse (n = 6, all males). **D** Representative confocal images showing Ki67⁺ (green) proliferating IBA1⁺ microglia (magenta) associated with 6E10⁺ A β plaques (red). DAPI (blue) marks the nuclei. The dotted boxes mark the insets. Graph shows quantification of the number of Ki67⁺ microglia per plaque averaged over 15 plaques per section with 3 sections per mouse (n = 5, all males). **E** Representative confocal images and Imaris-based 3D rendering of ThioS⁺ A β plaques (green), IBA1⁺ microglia (red), and CD68⁺ phagolysosomes (magenta). A β volume colocalized within the CD68 volume is shown as a separate channel (orange). Graphs show quantification of CD68 staining volume per plaque and the percentage of plaque volume engulfed in CD68 staining. 15 plaques per section with 3 sections per mouse were analysed (n = 6, all males). Statistical significance between experimental groups was calculated by one-way ANOVA with Tukey's post hoc test (A-B) and unpaired two-tailed Student's t-test (C-E). Error bars denote mean \pm SEM. ns: non-significant, * P < 0.05, ** P < 0.01, and *** P < 0.001

the other hand, downregulated biological processes were innate immune responses, interferon signaling, phagocytosis, defense response to pathogens, cytokine signaling, mitotic cell cycle and antigen presentation (Fig. 4D). Altogether, these results indicate that Asrij depletion predominantly increases expression of metabolism and mitochondrial activity genes with a concomitant reduction in innate immunity and proliferation genes in microglia, suggesting a protective response to A β pathology.

Activated microglia must maintain a high energy metabolism coupled with anabolic processes to counter A β pathology [30–32]. Asrij interacts with electron transport chain (ETC) components and regulates Complex I activity and Complex III assembly [7, 10]. Hence, we chose to investigate changes in mitochondrial activity in greater detail. Firstly, we analyzed the expression of genes that encode mitochondrial ETC complex proteins. AD/KO microglia exhibited upregulation of genes related to

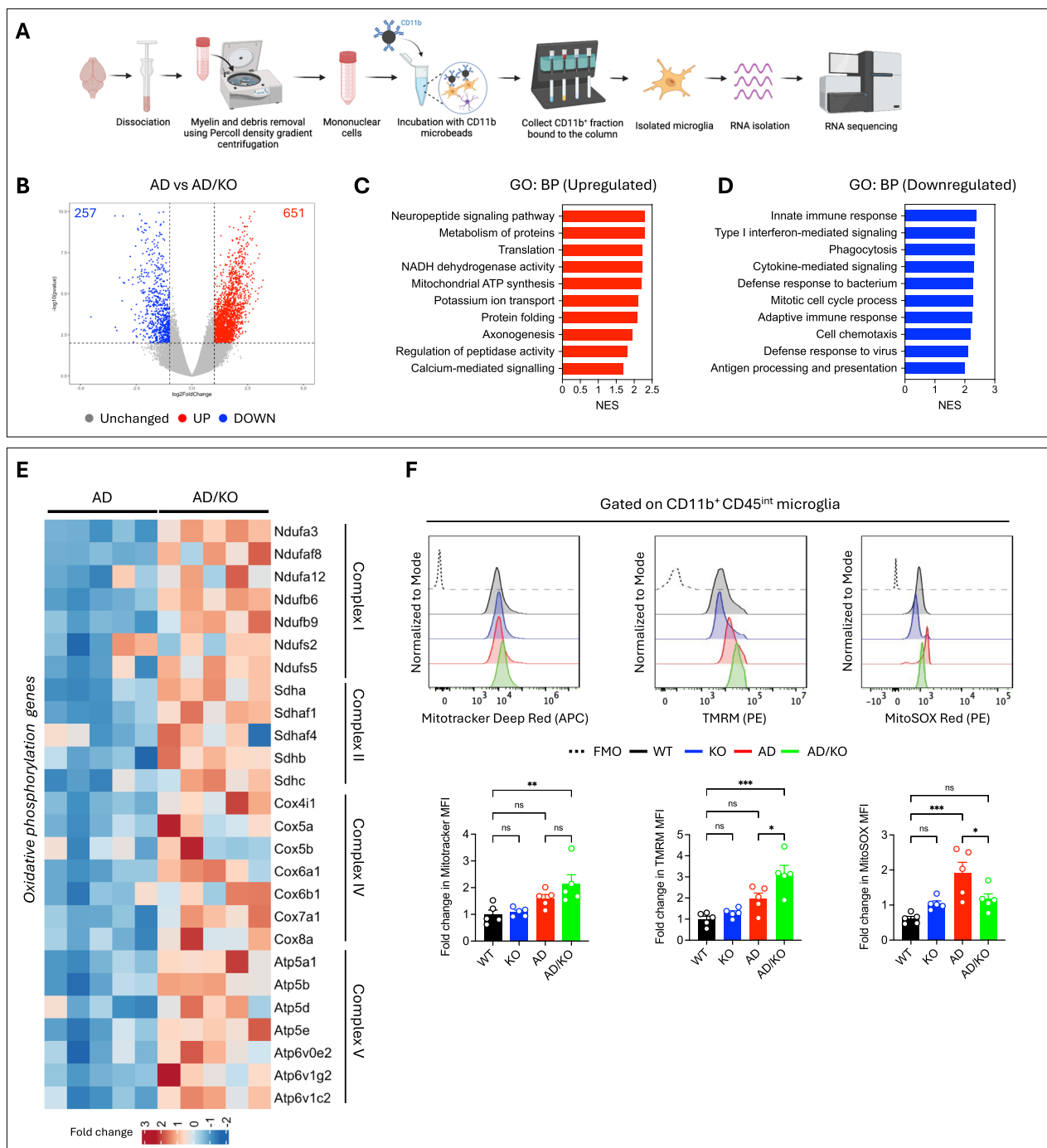


Fig. 4 Asrij deficiency upregulates metabolic genes and increases mitochondrial activity in AD microglia. **A** Schematic representing the experimental workflow of microglia isolation for RNA-seq analysis (n = 5 mice, all males). **B** Volcano plot depicting differentially expressed genes (DEGs). Points in red and blue are significantly ($P < 0.01$) upregulated ($\log_2FC > 1$) and downregulated ($\log_2FC < -1$) genes, respectively. **C** Bar graph shows top 10 significantly enriched gene ontology terms and their normalized enrichment score (NES) in upregulated DEGs (FDR < 0.05). **D** Bar graph shows top 10 significantly enriched gene ontology terms and their normalized enrichment score (NES) in downregulated DEGs (FDR < 0.05). **E** Heatmap of significantly upregulated ($P < 0.01$, $\log_2FC > 1$) genes involved in oxidative phosphorylation. **F** Representative histograms show flow cytometry analysis of Mitotracker Deep Red, TMRM, and MitoSOX Red staining in CD11b⁺ CD45^{int} microglia. Black dotted line represents fluorescence minus one (FMO) control. Graphs show quantification of fold change in median fluorescence intensity (MFI) of the indicated mitochondrial dyes (n = 5, all females). Statistical significance between experimental groups was calculated by two-sided Wald test (**B**), hypergeometric test (**C-D**) and one-way ANOVA with Tukey's post-hoc test (**F**). Error bars denote mean \pm SEM. ns- non-significant, * $P < 0.05$, ** $P < 0.01$, and *** $P < 0.001$

subunits of NADH dehydrogenase complex, succinate dehydrogenase, cytochrome c oxidase complex, and ATP synthase (Fig. 4E). Next, we performed flow cytometry to evaluate mitochondrial activity of CD11b⁺ CD45^{int} microglia using mitochondria specific dyes. AD/KO microglia had equivalent staining for Mitotracker Deep Red as compared to AD microglia, suggesting unchanged mitochondrial mass. Interestingly, we observed increased Tetramethylrhodamine, Methyl Ester, Perchlorate (TMRM) intensity in AD/KO microglia indicating increased mitochondrial membrane potential, an indicator of mitochondrial activity. Further, MitoSOX Red staining revealed reduced mitochondrial reactive oxygen species (ROS) in AD/KO microglia (Fig. 4F). Noticeably, lack of Asrij did not have any overt effect on the mitochondrial parameters in the absence of A β , suggesting that this could be an AD-specific response.

Upregulation of oxidative phosphorylation-related genes and mitochondrial activation is one of the hallmarks of mammalian target of rapamycin (mTOR) driven increase in microglial metabolism [35, 37]. Asrij negatively controls Akt activation in bone marrow cells [5]. Hence, we assessed the activation status of Akt-mTOR signaling. Immunoblotting analyses on magnetic bead-sorted CD11b⁺ cells demonstrated increased phosphorylation of Akt and mTOR in AD/KO microglia in comparison to AD microglia (Fig. S5B). Collectively, these data strongly indicate that Asrij negatively controls mitochondrial activity and the Akt-mTOR signaling axis. Thus, depletion of Asrij possibly promotes microglial metabolic fitness, resulting in a neuroprotective microglial response in AD.

Asrij promotes inflammatory disease-associated microglia (DAM) activation state

Upon sensing A β and inflammatory cues, microglia undergo dramatic morphological changes that reflect their activation status. Homeostatic/resting microglia typically exhibit a small soma with highly ramified processes. Microglial activation is accompanied by a shift to larger soma size and retraction of processes, resulting in the acquisition of an amoeboid morphology [29]. This morphological transition is pivotal for the subsequent microglial immune responses, such as phagocytosis and cytokine production that influence A β pathology [26, 38]. Since Asrij depletion reduced microglial activation, we analyzed microglial morphology. AD/KO microglia harbored fewer branches and had reduced total branch length, highlighting reduced morphological complexity compared to AD microglia. In contrast, WT and KO microglia did not exhibit any morphological changes (Fig. 5A). This illustrates that the effects of Asrij depletion on microglial morphology largely manifest in the presence of A β pathology. Thus, Asrij is pivotal for microglia to attain a morphologically activated state in AD.

Single-cell RNA profiling of AD mouse models has identified that microglia adopt a unique transcriptional profile to become disease-associated microglia (DAM), also referred to as microglial neurodegenerative phenotype (MGnD). This state is characterized by the downregulation of homeostatic markers and upregulation of genes involved in innate immune signaling, phagocytosis, lipid metabolism, and inflammation [28, 39, 40]. The downregulation of innate immune processes observed in our transcriptomic analysis spurred our interest to elucidate whether Asrij affects the acquisition of DAM transcriptional state in response to A β . Interestingly, among the most

(See figure on next page.)

Fig. 5 Asrij promotes inflammatory disease-associated microglia (DAM) activation state. **A** Representative renderings of the microglial skeleton using the 'filament' module of Imaris. Graphs show quantification of branch number per microglia and total branch length (n=3 for WT and KO, n=6 for AD and AD/KO, all males). **B** Heatmap of significantly downregulated ($P < 0.01$, $\log_2FC < -1$) genes belonging to DAM signature. **C** Representative confocal images showing DAM marker, CLEC7A (magenta) on IBA1⁺ microglia (red) associated with ThioS⁺ plaques (green). Graphs show quantification of percent CLEC7A⁺ area normalized to IBA1⁺ area and percent CLEC7A⁺ area per plaque averaged over 15 plaques per section with 3 sections per mouse (n=6, all males). **D** Representative confocal images showing homeostatic marker, TMEM119 (red) on IBA1⁺ microglia (magenta) associated with 6E10⁺ plaques (green). Graphs show quantification of percent TMEM119⁺ area normalized to IBA1⁺ area and percent TMEM119⁺ area per plaque averaged over 15 plaques per section with 3 sections per mouse (n=6, all males). **E, F** Heatmaps of significantly downregulated ($P < 0.01$, $\log_2FC < -1$) pro-inflammatory genes and IRM signature genes. **G, H, I** Graphs show quantification of IL-6, TNF- α and IL-1 β levels (pg/mL) in the hippocampus by ELISA (n=6, all males). **J** Bar graph shows the top 10 significantly downregulated MSigDB hallmark pathways ($P < 0.05$). **K** Immunoblot analysis of phospho-STAT3 (tyrosine 705) and STAT3 levels in CD11b⁺ microglia. GAPDH is loading control. Graph shows quantification of fold change in p-STAT3 normalized to total STAT3 (n=3, all females). **L** Immunoblot analysis of phospho-NF- κ B (serine 563) and NF- κ B levels in CD11b⁺ microglia. GAPDH is loading control. Graph shows quantification of fold change in p-NF- κ B normalized to total NF- κ B (n=3, all females). Statistical significance between experimental groups was calculated by one-way ANOVA with Tukey's post-hoc test (**A, G, H** and **K, L**), unpaired two-tailed Student's t-test (**C-D** and **I**), and Fischer exact test (**J**). Error bars denote mean \pm SEM. ns: non-significant, * $P < 0.05$, ** $P < 0.01$, and *** $P < 0.001$

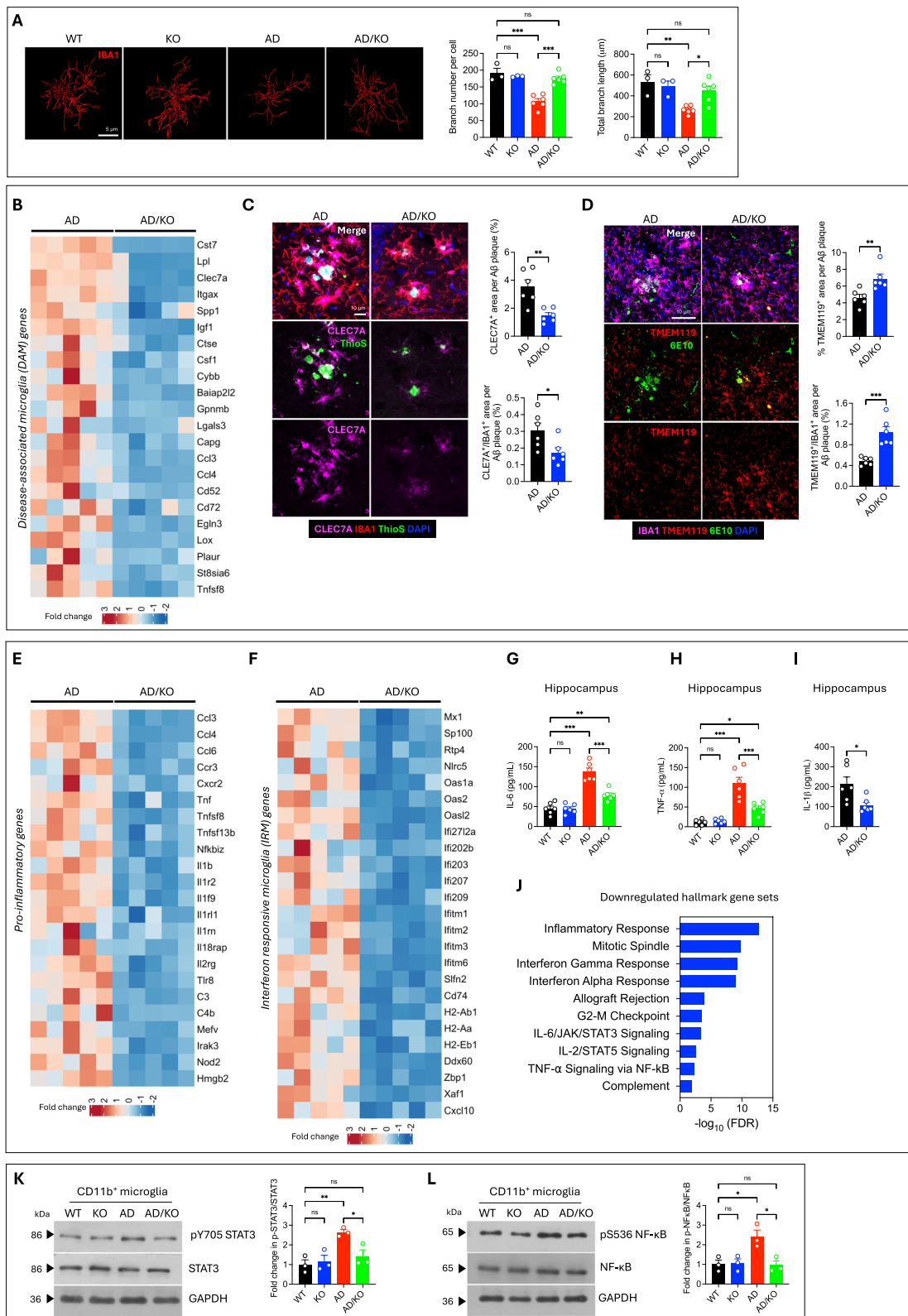


Fig. 5 (See legend on previous page.)

significantly downregulated were key genes involved in DAM phenotype, such as *Cst7*, *Lpl*, *Clec7a*, *Itgax*, *Csf1*, and *Ccl6* among others (Fig. 5B). We validated this block in DAM acquisition by evaluating levels of canonical DAM marker, C-Type lectin domain containing 7A (CLEC7A), on IBA1⁺ microglia surrounding A β plaques. AD/KO microglia expressed lower levels of CLEC7A than AD microglia (Fig. 5C). Also, DAM activation is accompanied by a reduction in the signature microglial homeostatic marker, transmembrane protein 119 (TMEM119) [39]. We found that plaque-proximal AD/KO microglia showed higher TMEM119 levels than those in AD mice, suggesting their retention in a more homeostatic state (Fig. 5D). Altogether, our transcriptomic and imaging results highlight a critical role of *Asrij* in the transformation of homeostatic microglia to DAM in response to A β .

DAM can mount a pro-inflammatory or anti-inflammatory response depending on the disease stage [37–39]. Inhibition of pro-inflammatory DAM response has been shown to reduce A β deposition and associated neuropathology in AD models [44–47]. Hence, we characterized inflammatory changes that may accompany the attenuated DAM state seen in AD/KO mice. The majority of the downregulated genes in AD/KO microglia consisted of pro-inflammatory chemokines and cytokines such as *Ccl4*, *Tnf*, *Il1b*, immune receptors, and associated accessory proteins such as *Tnfrsf8*, *Tnfrsf26*, *Il1r2*, *Il2rg*, pathogen recognition receptors including *Tlr8*, *Tlr11* and *Nod2* and complement factors, *C3* and *C4b* (Fig. 5E). Also, it was noteworthy, that 27 downregulated genes belong to the interferon response microglia (IRM) signature [48], such as the RNA recognition and binding factors, *Mx1*, *Oas2*, *Oas1a*, *Zbp1* and *Ddx60*, major histocompatibility complex (MHC) class II presentation such as *Cd74*, *H2-Ab1*, *H2-Aa*, and *H2-Eb1*, interferon-stimulated genes (ISGs) such as *Ifi2712a*, *Ifi204*, *Ifitm1*, *Ifitm6* and *Cxcl10* (Fig. 5F). To validate RNA-seq results, we measured the concentration of pro-inflammatory cytokines, interleukin-6 (IL-6), tumor necrosis factor α (TNF- α) and interleukin-1 β (IL-1 β) in the brain homogenates using ELISA. While *Asrij* depletion alone in the absence of A β pathology does not affect cytokine levels, AD/KO mice brains had substantially reduced levels of IL-6, TNF- α and IL-1 β as compared to AD mice (Fig. 5G–I). To identify which pathways are responsible for reduced inflammatory activation in *Asrij* deficient microglia, we performed pathway enrichment analysis on the downregulated DEGs using the molecular signatures database (MSigDB) hallmark gene set collection. This uncovered that interferon (IFN) gamma and alpha response, IL6/JAK/STAT3 signaling, TNF- α /NF- κ B signaling, and IL-2/STAT5 signaling were significantly

downregulated in AD/KO microglia (Fig. 5J). To validate reduced inflammatory pathway activation, we carried out immunoblotting analyses on MACS-sorted CD11b⁺ microglia. AD/KO microglia showed reduced levels of phosphorylated STAT3 and NF- κ B, confirming the inhibition of inflammatory signaling (Fig. 5K–L). Taken together, these studies clearly demonstrate that *Asrij* depletion induces a shift to a less immunogenic and dampened pro-inflammatory microglial activation profile.

Discussion

Alzheimer's disease (AD) is a complex, multifactorial and progressive disease. An increase in *Asrij* levels in the brain positively correlates with the severity of AD pathology in mice and humans [4]. Previous reports showed that primary neurons that are exposed to A β in vitro, upregulate *Asrij* and undergo mitochondria-mediated apoptosis, whereas *Asrij* depletion from neurons reduced A β -induced apoptosis [4]. Hence, it is tempting to speculate a neuronal role for *Asrij* in neurodegeneration in AD. However, the role of *Asrij* in glial activation and neuroinflammation, which are among the most critical factors that modify the disease outcome, is not known. This necessitates a comprehensive analysis of the role of *Asrij* on AD pathology and progression, in an in vivo setting, that faithfully recapitulates the nuances of A β pathology. Therefore, we asked whether reducing *Asrij* levels in vivo is sufficient to mitigate the disease. Here, we show that *Asrij* depletion in the *APP/PS1* mice restores cognitive functions, reduces A β burden and neuronal damage, and decreases reactive astrogliosis. Mechanistically, *Asrij* suppresses mitochondrial activity and promotes neuroinflammatory signaling in AD microglia. Thus, increased *Asrij* in AD leads to microglial dysregulation and exacerbates A β pathology and cognitive dysfunction in mice (Fig. 6).

Asrij regulates myeloid cell homeostasis and innate immune responses in *Drosophila* and mice. Further, *Asrij* is upregulated in AD microglia, suggesting that it has a role in microglial responses to A β pathology. We demonstrate that *Asrij* deletion significantly dampens microglial activation, as seen by reduced microgliosis and lesser microglial clustering around plaques. From the available reports, it is unclear whether microglial activation protects from AD progression or is detrimental of both. Activated microglia are necessary for A β phagocytosis and clearance, but can also propagate neuronal death and inflammation, via the production of cytokines [49]. Also, complement-mediated aberrant synaptic pruning by activated microglia, contributes to excessive synaptic loss in AD [24]. Microglia-driven neuroinflammation can further accelerate A β deposition

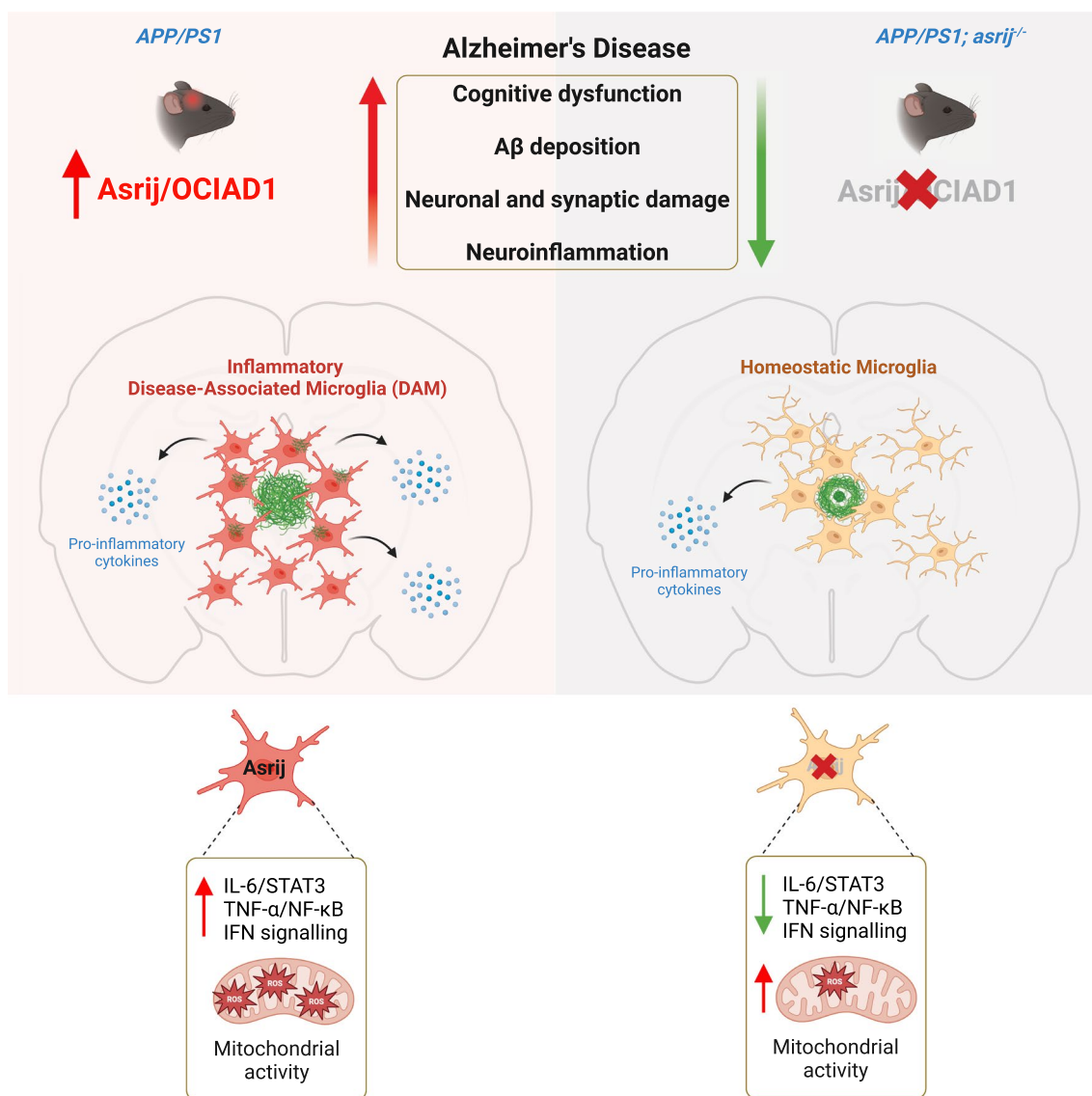


Fig. 6 Graphical summary of the role of Asrij in microglial inflammatory activation and AD pathophysiology. Asrij promotes activation of inflammatory signalling pathways in AD microglia and thus exacerbates neuroinflammation and AD pathology. Hence, Asrij depletion curtails microglial activation and associated neuropathology to ameliorate cognitive dysfunction in AD

[50]. Given that AD/KO mice exhibit reduced Aβ plaques, it appears that reduced microglial activation and plaque association may be protective in this context, as opposed to other cases such as loss of TREM2, SYK, or VPS35, which leads to increased plaque burden and worsens AD pathology [15, 37, 51].

Asrij depletion leads to diminished microglial Aβ uptake and phagocytosis activation, with a concomitant reduction of Aβ burden. Though this finding may seem counter-intuitive, it is not surprising, given the growing evidence of poor correlation between microglial phagocytosis and plaque load [52]. Recent studies

have shown that microglial phagocytosis may, in fact, act to 'build' plaques rather than dismantle them. For example, the deletion of phagocytic receptors, Axl and Mer, in microglia, leads to an overall reduction of dense core plaques [30]. Genetic or pharmacological depletion of microglia reduces plaque deposition [53–55]. On the other hand, CARD9 deletion increases microgliosis as well as Aβ burden [14]. Microglia also help seed and spread plaques, thus contributing to AD pathology [31, 56]. We found that Asrij deficient AD mice showed no change in plaque burden at 5 months of age, but had diminished Aβ plaque load and reduced

plaque size from 10 months of age. It is well known continual accumulation of A β instigates the activation of inflammatory signaling and NLRP3 inflammasomes. The release of inflammasome-mediated apoptosis-associated speck-like protein containing a CARD (ASC) specks can cross-seed A β and enhance plaque growth. Abrogating neuroinflammation by deletion of Nlrp3 or ASC does not affect plaque load at early stages of disease (4–5 months) but reduces plaque load at later stages (8–16 months) [56–58]. Similarly, TREM2 deletion does not affect plaque load in 6 month-old PS2APP mice but reduces late-stage amyloid accumulation (12 month-old), possibly by attenuating neuroinflammation [59]. Given that Asrij promotes microglia-driven neuroinflammation, its depletion has a more profound effect at late stages (10 months) than at the early phase of A β deposition (5 months). We speculate that *asrij* deletion may limit neuroinflammation-mediated A β deposition and plaque growth. Therefore, it is likely that we do not observe any effect on A β load in 5 month-old AD/KO mice, where neuroinflammation has not been set to a sufficient extent due to moderate A β load. We found reduced microglial NF- κ B activation and decreased IL-1 β levels in the AD/KO brain, which suggests attenuated inflammasome activation. Whether and how Asrij regulates inflammasome activation in microglia warrants further investigation. Thus, it is tempting to speculate that Asrij may promote neuroinflammation-assisted plaque deposition and growth, as well as A β spread.

Plaque-associated microglia must maintain metabolic fitness, by upregulating energy metabolism and cellular biosynthetic pathways, to counter AD pathology [60, 61]. The extent of microglial metabolic dysfunction is a critical determinant of neuroinflammatory responses in AD [62, 63]. Our RNA-seq analysis reveals that Asrij depletion induces a unique transcriptional shift in AD microglia, marked predominantly by the upregulation of mitochondrial metabolism genes. Increased mitochondrial activity is particularly interesting, in light of previous studies linking Asrij to mitochondrial homeostasis. Asrij, an inner mitochondrial membrane protein, regulates mitochondrial dynamics and energy metabolism [64, 65]. It interacts with mitochondrial ETC complexes and negatively regulates Complex I activity, thus restraining oxidative phosphorylation [7]. We hypothesize that Asrij depletion may alleviate this repression of mitochondrial activity and provide the energy boost required to maintain microglial metabolic fitness. However, the molecular mechanism by which Asrij controls microglial mitochondrial homeostasis warrants further investigation.

Single-cell RNA sequencing studies have uncovered that homeostatic microglia undergo a transcriptional

shift to become DAM/MGnD during neurodegenerative diseases, chronic inflammation and aging [66]. Our transcriptome analysis shows that Asrij facilitates the transition to the DAM state, as DAM signature genes and signaling pathways are dramatically downregulated in AD/KO mice. DAM are believed to be neuroprotective owing to their enhanced phagocytic and clearance functions [66]. However, studies in AD mouse models have yielded confounding results, with reduced DAM resulting in either enhanced or reduced neuropathology. This may be because, under conditions of chronic inflammation, DAM get dysregulated and can be pro-inflammatory, anti-inflammatory, or a combination of both [67]. For example, deletion of RIPK3, which reduces microglial pro-inflammatory activation, is accompanied by attenuated DAM and reduced A β pathology [44, 45]. Similarly, microglial cGAS deletion ameliorated neuroinflammation by inhibiting DAM emergence [46]. Our study shows that Asrij is critical for the development of a pro-inflammatory DAM state. This is explained by the downregulation of several signaling pathways that contribute to inflammatory microglial activation. It is compelling that Asrij deficiency inhibited the interferon response microglia (IRM) profile, as observed by the remarkable reduction of IFN signaling genes. Hyperactive IFN signaling enhances neuroinflammation, synapse loss, and cognitive decline in AD [47]. We also found reduced levels of pro-inflammatory cytokines in the brain milieu of AD/KO mice, suggesting reduced neuroinflammation. As neuroinflammation has been shown to aggravate A β pathology and cognitive impairments, it is reasonable to conclude that Asrij-dependent inflammatory microglial activation may contribute to AD progression. Mechanistically, Asrij acts as a scaffold protein to regulate multiple signaling pathways essential for immune homeostasis in *Drosophila* and mice [64]. A similar function of Asrij, may be adapted in AD to fine-tune the immune signaling required for microglial activation. Given that our RNA-seq analysis revealed dramatic neuroinflammatory changes in microglia, we believe that the effects on AD pathology are, at least in part, driven by microglia-intrinsic functions, which may be confirmed by microglia-specific Asrij depletion. Additionally, our approach of using CD11b microbeads to isolate microglia will also enrich other myeloid cells in the brain. It is possible that some of the transcriptomic results may also reflect changes in brain resident myeloid cells. While Asrij knockout before disease onset retards AD progression, it will be interesting to see whether reducing Asrij levels after disease onset, may retard or ameliorate AD phenotypes.

Multiple studies have demonstrated the complexity of AD pathology, which depends on the gene affected, cell

type and disease context. Several germline mutations in microglia-enriched genes that are implicated in AD may also affect peripheral immune cells. While modulation of microglial activation could be a promising therapeutic strategy, as many of the AD-related microglial receptors and signaling pathways are shared by peripheral myeloid cells, this could lead to undesirable effects [50]. For example, the role of TREM2 in A β pathology is unclear. While one report indicates that TREM2 knockout reduces inflammatory macrophages and ameliorates A β pathology [68] another demonstrates that TREM2 knockout reduces microglial activation and increases A β pathology [59]. Similarly, inhibiting SHIP-1 signaling leads to distinct effects depending on the disease stage and whether targeting is microglia-specific or pan-myeloid [69]. These seemingly conflicting results highlight the importance of studying the role of molecular regulators in microglia, as well as in peripheral immune cells for safe and effective microglia-targeted AD therapies. Our study emphasizes that a tight balance of *Asrij* levels is essential for the coordination of its multiple roles. While increased *Asrij* levels promote AD, reducing *Asrij* levels in non-AD mice promotes uncontrolled myeloproliferation in the bone marrow. Here, we show that though *Asrij* maintains myeloid cell and mitochondrial homeostasis, it has a divergent role of immune activation in microglia. Therefore, our study uncovers a novel mechanism of *Asrij*-dependent microglial dysfunction that drives neuroinflammatory microglial responses. It is important to note that the AD risk and the extent of neuropathology and cognitive decline is sex-dependent. Females are at a higher risk of developing AD compared to males. This is also reflected in several AD mouse models wherein female mice accumulate A β pathology earlier and to a greater severity as compared to male mice. Interestingly, sexual dimorphism in AD microglia could be one of the intrinsic factors. Whether *Asrij* expression and its depletion phenotypes show sex-dependent changes in AD will be an interesting aspect to study in future. Our approach of using a whole-body *asrij* KO mice does not allow microglia-specific effects to be discerned. As *Asrij* is expressed in neurons, astrocytes, oligodendrocytes and other immune cells, it is not possible to exclude potential effects of *Asrij* depletion on these cell types, which appreciably modulate AD pathology. Our study lays foundation to now evaluate microglia-intrinsic role of *Asrij* in AD progression using microglia specific mouse Cre driver lines. This will also help tease out the contribution of systemic inflammatory responses and microglia-driven impact of *Asrij* in AD. Given the diverse functions of *Asrij*, therapeutic modulation of its levels in AD will likely result in distinct clinical outcomes, based

on the disease stage and systemic responses. Our study gives insights into microglial biology that could help devise strategies to prevent or retard AD progression and improve clinical outcomes.

Conclusions

In summary, we show that *Asrij* depletion ameliorates A β pathology, neuronal and synaptic damage and gliosis, and improves behavioral performance in *APP/PS1* mice. *Asrij* suppresses microglial mitochondrial activity and promotes the development of DAM, which likely leads to worsening of AD pathology with increase in *Asrij* levels. Depleting *Asrij* in an AD context limits neuroinflammatory signaling activation in microglia, enabling neuroprotective microglial responses. Collectively, our findings show that reducing *Asrij* levels may help retard AD. Our work positions *Asrij* as a critical molecular regulator that links microglial dysfunction to AD pathogenesis.

Abbreviations

AD	Alzheimer's disease
A β	Amyloid beta
GWAS	Genome-wide association studies
OClAD1	Ovarian carcinoma immunoreactive antigen domain protein 1
GSK3 β	Glycogen synthase kinase 3 beta
DAM	Disease-associated microglia
WT	Wild type
KO	Knockout
PCR	Polymerase chain reaction
JNCASR	Jawaharlal Nehru Centre for Advanced Scientific Research
OFT	Open field test
MWM	Morris water maze
PBS	Phosphate-buffered saline
PFA	Paraformaldehyde
RNA	Ribonucleic acid
RT	Room temperature
FBS	Fetal bovine serum
DAPI	4',6-Diamidino-2-phenylindole
HEPES	4-(2-Hydroxyethyl)-1-piperazineethanesulfonic acid
EDTA	Ethylenediaminetetraacetic acid
DTT	Dithiothreitol
PMSF	Phenylmethylsulfonyl fluoride
SDS	Sodium dodecyl sulfate
HRP	Horseradish peroxidase
ECL	Clarity western enhanced chemiluminescence
HBSS	Hanks' balanced salt solution
BSA	Bovine serum albumin
DPBS	Dulbecco's phosphate-buffered saline
MACS	Magnetic-activated cell sorting
FACS	Fluorescence-activated cell sorting
TMRM	Tetramethylrhodamine, Methyl Ester, Perchlorate
FSC-A	Forward scatter area
SSC-A	Side scatter area
FSC-H	Forward scatter height
SSC-W	Side scatter width
MFI	Median fluorescence intensity
IMDM	Iscove's modified Dulbecco's medium
ELISA	Enzyme-linked immunosorbent assay
RT-qPCR	Reverse transcription-quantitative polymerase chain reaction
QC	Quality control
rRNA	Ribosomal RNA
PCA	Principal component analysis
MSigDB	Molecular signatures database

SEM	Standard error of mean
ANOVA	Analysis of variance
ThioS	Thioflavin S
APP	Amyloid precursor protein
CTF	Carboxy-terminal fragments
LAMP1	Lysosomal-associated membrane protein 1
PSD95	Post synaptic density 95
GFAP	Glial fibrillary acidic protein
S100B	S100 calcium-binding protein B
IBA1	Ionized calcium-binding adapter molecule 1
CD68	Cluster of differentiation 68
RNA-seq	RNA sequencing
GO	Gene ontology
DEG	Differentially expressed genes
TMRM	Tetramethylrhodamine, Methyl Ester, Perchlorate
ROS	Reactive oxygen species
mTOR	Mammalian target of rapamycin
Mgnd	Microglial neurodegenerative phenotype
CLEC7A	C-Type lectin domain containing 7A
TMEM119	Transmembrane protein 119
IRM	Interferon response microglia
ISG	Interferon-stimulated genes
MHC	Major histocompatibility complex
IL-6	Interleukin-6
TNF-alpha	Tumor necrosis factor α
IL-1beta	Interleukin-1 β
IFN	Interferon
KEGG	Kyoto encyclopedia of genes and genomes
GAPDH	Glyceraldehyde-3-phosphate dehydrogenase
STAT3	Signal transducer and activator of transcription 3
NF-kB	Nuclear factor kappa-light-chain-enhancer of activated B cells
ETC	Electron transport chain
BLISc	Bangalore life science cluster

Supplementary Information

The online version contains supplementary material available at <https://doi.org/10.1186/s12974-025-03415-5>.

Supplementary Material 1.

Acknowledgements

The authors thank members of Inamdar laboratory for valuable suggestions; Aishwarya Prakash for RNA-seq data analysis; Dr. Ashish Kumar for help with mice maintenance; Milind Kumar Anand for help with imaging; Hiyaa Ghosh lab at the National Centre for Biological Sciences (NCBS), Bangalore for help with reagents and protocols; Bioimaging, flow cytometry and animal facilities at JNCASR. Graphical abstract and schematics were prepared using BioRender.

Author contributions

Conceptualization: P.D, T.G.R and M.S.I. methodology, experiments, and data analysis: P.D and M.R. data discussions: P.D, M.R., T.G.R and M.S.I. writing—original draft: P.D. and M.S.I. writing—review and editing: P.D, M.R., T.G.R, M.S.I. funding acquisition and resources: M.S.I and T.G.R.

Funding

This work was supported by funding to M.S.I and T.G.R from the Science and Engineering Research Board (SERB) (CRG/2021/003566) and intramural funds from Jawaharlal Nehru Centre for Advanced Scientific Research (JNCASR) and Institute for Stem Cell Science and Regenerative Medicine (inStem). T.G.R is also funded by SERB (CRG/2020/004594). M.S.I is also funded by JC Bose fellowship (JCB/2019/000020), Department of Science and Technology, Government of India.

Availability of data and materials

All data supporting the findings of this study are available in the paper and its supplementary figures. All the original raw data and analysis files are available with the corresponding authors upon reasonable request. RNA sequencing

data has been deposited into the gene expression omnibus (GEO) database under accession number GSE272625.

Declarations

Ethics approval and consent to participate

All mice experiments were approved by the JNCASR institutional animal ethics committee (project #MSI012) and were conducted in accordance with the standard guidelines. This work did not involve the use of material from human subjects.

Consent for publication

All authors have read and approved the final manuscript for publication.

Competing interests

The authors declare no competing interests.

Author details

¹Molecular Biology and Genetics Unit, Jawaharlal Nehru Centre for Advanced Scientific Research (JNCASR), Bangalore, Karnataka 560064, India. ²Bioorganic Chemistry Laboratory, New Chemistry Unit, Jawaharlal Nehru Centre for Advanced Scientific Research (JNCASR), Bangalore, Karnataka 560064, India. ³Institute for Stem Cell Science and Regenerative Medicine (inStem), Bangalore, Karnataka 560065, India.

Received: 19 January 2025 Accepted: 10 March 2025

Published online: 20 March 2025

References

- Govindaraju T, editor. Alzheimer's disease: recent findings in pathophysiology, diagnostic and therapeutic modalities. Cambridge: Royal Society of Chemistry; 2022.
- Ramesh M, Govindaraju T. Multipronged diagnostic and therapeutic strategies for Alzheimer's disease. *Chem Sci*. 2022;13(46):13657–89.
- Andrews SJ, Renton AE, Fulton-Howard B, Podlesny-Drabiniok A, Marcora E, Goate AM. The complex genetic architecture of Alzheimer's disease: novel insights and future directions. *EBioMedicine*. 2023;90: 104511.
- Li X, Wang L, Cykowski M, He T, Liu T, Chakranarayan J, et al. OCIAD1 contributes to neurodegeneration in Alzheimer's disease by inducing mitochondrial dysfunction, neuronal vulnerability and synaptic damages. *EBioMedicine*. 2020;51: 102569.
- Sinha S, Dwivedi TR, Yengkhom R, Bheemsetty VA, Abe T, Kiyonari H, et al. *Asrij*/OCIAD1 suppresses CSN5-mediated p53 degradation and maintains mouse hematopoietic stem cell quiescence. *Blood*. 2019;133(22):2385–400.
- Sinha A, Khadilkar RJ, Vinay KS, Sinha AR, Inamdar MS. Conserved regulation of the JAK/STAT pathway by the endosomal protein *Asrij* maintains stem cell potency. *Cell Rep*. 2013;4(4):649–58.
- Shetty DK, Kalamkar KP, Inamdar MS. OCIAD1 controls electron transport chain complex I activity to regulate energy metabolism in human pluripotent stem cells. *Stem Cell Rep*. 2018;11(1):128–41.
- Sinha S, Sinha A, Dongre P, Kamat K, Inamdar MS. Organelle dysfunction upon *asrij* depletion causes aging-like changes in mouse hematopoietic stem cells. *Aging Cell*. 2022;21(4): e13570.
- Kulkarni V, Khadilkar RJ, Magadi SS, Inamdar MS. *Asrij* maintains the stem cell niche and controls differentiation during *Drosophila* lymph gland hematopoiesis. *PLoS ONE*. 2011;6(11): e27667.
- Le Vasseur M, Friedman J, Jost M, Xu J, Yamada J, Kampmann M, et al. Genome-wide CRISPRi screening identifies OCIAD1 as a prohibitin client and regulatory determinant of mitochondrial complex III assembly in human cells. *Elife*. 2021;26(10): e67624.
- Khadilkar RJ, Ray A, Chetan DR, Sinha AR, Magadi SS, Kulkarni V, et al. Differential modulation of the cellular and humoral immune responses in *Drosophila* is mediated by the endosomal ARF1-*Asrij* axis. *Sci Rep*. 2017;7(1):118.

12. Uhlén M, Fagerberg L, Hallström BM, Lindskog C, Oksvold P, Mardinoglu A, et al. Proteomics. Tissue-based map of the human proteome. *Science*. 2015;347(6220):1260419.
13. Samanta S, Rajasekhar K, Ramesh M, Murugan NA, Alam S, Shah D, et al. Naphthalene monoimide derivative ameliorates amyloid burden and cognitive decline in a transgenic mouse model of Alzheimer's disease. *Adv Ther*. 2021;4(4):2000225.
14. Ennerfelt H, Holliday C, Shapiro DA, Zengeler KE, Bolte AC, Ulland TK, et al. CARD9 attenuates A β pathology and modifies microglial responses in an Alzheimer's disease mouse model. *Proc Natl Acad Sci USA*. 2023;120(24):e2303760120.
15. Ennerfelt H, Frost EL, Shapiro DA, Holliday C, Zengeler KE, Voithofer G, et al. SYK coordinates neuroprotective microglial responses in neurodegenerative disease. *Cell*. 2022;185(22):4135–4152.e22.
16. Chen S, Zhou Y, Chen Y, Gu J. fastp: an ultra-fast all-in-one FASTQ preprocessor. *Bioinformatics*. 2018;34(17):i884–90.
17. Graph-based genome alignment and genotyping with HISAT2 and HISAT-genotype. *Nat Biotechnol*. <https://www.nature.com/articles/s41587-019-0201-4>. Accessed 3 Oct 2024.
18. Li H, Handsaker B, Wysoker A, Fennell T, Ruan J, Homer N, et al. The sequence Alignment/Map format and SAMtools. *Bioinformatics*. 2009;25(16):2078–9.
19. featureCounts: an efficient general purpose program for assigning sequence reads to genomic features. *Bioinformatics*. Oxford Academic. <https://academic.oup.com/bioinformatics/article/30/7/923/232889>. Accessed 3 Oct 2024.
20. Love MI, Huber W, Anders S. Moderated estimation of fold change and dispersion for RNA-seq data with DESeq2. *Genom Biol*. 2014;15(12):550.
21. Kuleshov MV, Jones MR, Rouillard AD, Fernandez NF, Duan Q, Wang Z, et al. Enrichr: a comprehensive gene set enrichment analysis web server 2016 update. *Nucl Acid Res*. 2016;44(W1):W90–97.
22. Ferguson SA, Sarkar S, Schmued LC. Longitudinal behavioral changes in the APP/PS1 transgenic Alzheimer's disease model. *Behav Brain Res*. 2013;242:125–34.
23. Radde R, Bolmont T, Kaeser SA, Coomaraswamy J, Lindau D, Stoltze L, et al. Abeta42-driven cerebral amyloidosis in transgenic mice reveals early and robust pathology. *EMBO Rep*. 2006;7(9):940–6.
24. Leng F, Edison P. Neuroinflammation and microglial activation in Alzheimer disease: where do we go from here? *Nat Rev Neurol*. 2021;17(3):157–72.
25. Escartin C, Galea E, Lakatos A, O'Callaghan JP, Petzold GC, Serrano-Pozo A, et al. Reactive astrocyte nomenclature, definitions, and future directions. *Nat Neurosci*. 2021;24(3):312–25.
26. Yuan P, Condello C, Keene CD, Wang Y, Bird TD, Paul SM, et al. TREM2 haploinsufficiency in mice and humans impairs the microglia barrier function leading to decreased amyloid compaction and severe axonal dystrophy. *Neuron*. 2016;90(4):724–39.
27. Hansen DV, Cullimore BK, Johanson JC, Cheng W. Chapter 8, microglial blockade of the amyloid cascade: a new therapeutic frontier. In: Govindaraju T, editor. *Alzheimer's disease*. Cambridge: Royal Society of Chemistry; 2022. p. 193–254.
28. Krasemann S, Madore C, Cialic R, Baufeld C, Calcagno N, Fatimy RE, et al. The TREM2-APOE pathway drives the transcriptional phenotype of dysfunctional microglia in neurodegenerative diseases. *Immunity*. 2017;47(3):566–581.e9.
29. Condello C, Yuan P, Grutzendler J. Microglia-mediated neuroprotection, TREM2, and Alzheimer's disease: evidence from optical imaging. *Biol Psychiat*. 2018;83(4):377–87.
30. Huang Y, Happonen KE, Burrola PG, O'Connor C, Hah N, Huang L, et al. Microglia use TAM receptors to detect and engulf amyloid β plaques. *Nat Immunol*. 2021;22(5):586–94.
31. d'Errico P, Ziegler-Waldkirch S, Aires V, Hoffmann P, Mezö C, Erny D, et al. Microglia contribute to the propagation of A β into unaffected brain tissue. *Nat Neurosci*. 2022;25(1):20–5.
32. Fruhwürth S, Zetterberg H, Paludan SR. Microglia and amyloid plaque formation in Alzheimer's disease—evidence, possible mechanisms, and future challenges. *J Neuroimmunol*. 2024;390: 578342.
33. Wang Y, Ulland TK, Ulrich JD, Song W, Tzaferis JA, Hole JT, et al. TREM2-mediated early microglial response limits diffusion and toxicity of amyloid plaques. *J Exp Med*. 2016;213(5):667–75.
34. Baik SH, Kang S, Lee W, Choi H, Chung S, Kim JI, et al. A breakdown in metabolic reprogramming causes microglia dysfunction in Alzheimer's disease. *Cell Metab*. 2019;30(3):493–507.e6.
35. Ulland TK, Song WM, Huang SCC, Ulrich JD, Sergushichev A, Beatty WL, et al. TREM2 maintains microglial metabolic fitness in Alzheimer's disease. *Cell*. 2017;170(4):649–663.e13.
36. March-Díaz R, Lara-Ureña N, Romero-Molina C, Heras-Garvin A, Ortega-de San Luis C, Alvarez-Vergara MI, et al. Hypoxia compromises the mitochondrial metabolism of Alzheimer's disease microglia via HIF1. *Nat Aging*. 2021;1(4):385–99.
37. Wang S, Sudan R, Peng V, Zhou Y, Du S, Yuede CM, et al. TREM2 drives microglia response to amyloid- β via SYK-dependent and -independent pathways. *Cell*. 2022;185(22):4153–4169.e19.
38. Javanmehr N, Saleki K, Aljanzadeh P, Rezaei N. Microglia dynamics in aging-related neurobehavioral and neuroinflammatory diseases. *J Neuroinflammation*. 2022;19(1):273.
39. Keren-Shaul H, Spinrad A, Weiner A, Matcovitch-Natan O, Dvir-Szternfeld R, Ulland TK, et al. A unique microglia type associated with restricting development of Alzheimer's disease. *Cell*. 2017;169(7):1276–1290.e17.
40. Sala Frigerio C, Wolfs L, Fattorelli N, Thrupp N, Voytyuk I, Schmidt I, et al. The major risk factors for Alzheimer's disease: age, sex, and genes modulate the microglia response to A β plaques. *Cell Rep*. 2019;27(4):1293–1306.e6.
41. Rangaraju S, Dammer EB, Raza SA, Rathakrishnan P, Xiao H, Gao T, et al. Identification and therapeutic modulation of a pro-inflammatory subset of disease-associated-microglia in Alzheimer's disease. *Mol Neurodegener*. 2018;13(1):24.
42. Gao T, Jernigan J, Raza SA, Dammer EB, Xiao H, Seyfried NT, et al. Transcriptional regulation of homeostatic and disease-associated-microglial genes by IRF1, LXR β , and CEBP α . *Glia*. 2019;67(10):1958–75.
43. Wang H. Microglia heterogeneity in Alzheimer's disease: insights from single-cell technologies. *Front Synaptic Neurosci*. 2021;23(13): 773590.
44. Kumar S, Budhathoki S, Oliveira CB, Kahle AD, Calhan OY, Lukens JR, et al. Role of the caspase-8/RIPK3 axis in Alzheimer's disease pathogenesis and A β -induced NLRP3 inflammasome activation. *JCI Insight*. 2023;8(3): e157433.
45. Ofengeim D, Mazzitelli S, Ito Y, DeWitt JP, Mifflin L, Zou C, et al. RIPK1 mediates a disease-associated microglial response in Alzheimer's disease. *Proc Natl Acad Sci U S A*. 2017;114(41):E8788–97.
46. Gulen MF, Samson N, Keller A, Schwabenland M, Liu C, Glück S, et al. cGAS–STING drives ageing-related inflammation and neurodegeneration. *Nature*. 2023;620(7973):374–80.
47. Roy ER, Wang B, Wan YW, Chiu G, Cole A, Yin Z, et al. Type I interferon response drives neuroinflammation and synapse loss in Alzheimer disease. *J Clin Investig*. 2020;130(4):1912–30.
48. Mathys H, Adai KK, Gao F, Young JZ, Manet E, Hemberg M, et al. Temporal tracking of microglia activation in neurodegeneration at single-cell resolution. *Cell Rep*. 2017;21(2):366–80.
49. Ramesh M, Balachandra C, Andhare P, Govindaraju T. Rationally designed molecules synergistically modulate multifaceted A β toxicity, microglial activation, and neuroinflammation. *ACS Chem Neurosci*. 2022;13(14):2209–21.
50. Samuels JD, Lukens JR, Price RJ. Emerging roles for ITAM and ITIM receptor signaling in microglial biology and Alzheimer's disease-related amyloidosis. *J Neurochem*. 2023. <https://doi.org/10.1111/jnc.15981>.
51. Ren X, Yao L, Wang Y, Mei L, Xiong WC. Microglial VPS35 deficiency impairs A β phagocytosis and A β -induced disease-associated microglia, and enhances A β associated pathology. *J Neuroinflammation*. 2022;19(1):61.
52. Daniels MJ, Lefevre L, Szymkowiak S, Drake A, McCulloch L, Tzioras M, et al. Cystatin F (Cst7) drives sex-dependent changes in microglia in an amyloid-driven model of Alzheimer's disease. *Elife*. 2023;12:e85279.
53. Spangenberg E, Severson PL, Hohsfield LA, Crasper J, Zhang J, Burton EA, et al. Sustained microglial depletion with CSF1R inhibitor impairs parenchymal plaque development in an Alzheimer's disease model. *Nat Commun*. 2019;10(1):3758.
54. Olmos-Alonso A, Schettler STT, Sri S, Askew K, Mancuso R, Vargas-Caballero M, et al. Pharmacological targeting of CSF1R inhibits microglial proliferation and prevents the progression of Alzheimer's-like pathology. *Brain*. 2016;139(3):891–907.

55. Casali BT, MacPherson KP, Reed-Geaghan EG, Landreth GE. Microglia depletion rapidly and reversibly alters amyloid pathology by modification of plaque compaction and morphologies. *Neurobiol Dis.* 2020;142:104956.
56. Venegas C, Kumar S, Franklin BS, Dierkes T, Brinkschulte R, Tejera D, et al. Microglia-derived ASC specks crossseed amyloid- β in Alzheimer's disease. *Nature.* 2017. <https://doi.org/10.1038/nature25158>.
57. McManus RM, Komes MP, Griep A, Santarelli F, Schwartz S, Ramón Perea J, et al. NLRP3-mediated glutaminolysis controls microglial phagocytosis to promote Alzheimer's disease progression. *Immunity.* 2025;58(2):326-343.e11.
58. Heneka MT, Kummer MP, Stutz A, Delekate A, Schwartz S, Vieira-Saecker A, et al. NLRP3 is activated in Alzheimer's disease and contributes to pathology in APP/PS1 mice. *Nature.* 2013;493(7434):674–8.
59. Meilandt WJ, Ngu H, Gogineni A, Lalehzadeh G, Lee SH, Srinivasan K, et al. Trem2 deletion reduces late-stage amyloid plaque accumulation, elevates the A β 42:A β 40 ratio, and exacerbates axonal dystrophy and dendritic spine loss in the PS2APP Alzheimer's mouse model. *J Neurosci.* 2020;40(9):1956–74.
60. Lepiarz-Raba I, Gbadamosi I, Florea R, Paolicelli RC, Jawaid A. Metabolic regulation of microglial phagocytosis: implications for Alzheimer's disease therapeutics. *Transl Neurodegener.* 2023;12(1):48.
61. Wang Q, Lu M, Zhu X, Gu X, Zhang T, Xia C, et al. The role of microglia immunometabolism in neurodegeneration: focus on molecular determinants and metabolic intermediates of metabolic reprogramming. *Biomed Pharmacother.* 2022;153:113412.
62. Codocedo JF, Mera-Reina C, Bor-Chian Lin P, Fallen PB, Puntambekar SS, Casali BT, et al. Therapeutic targeting of immunometabolism reveals a critical reliance on hexokinase 2 dosage for microglial activation and Alzheimer's progression. *Cell Rep.* 2024;43(7):114488.
63. Fairley LH, Wong JH, Barron AM. Mitochondrial regulation of microglial immunometabolism in Alzheimer's disease. *Front Immunol.* 2021;25(12):624538.
64. Praveen W, Sinha S, Batabyal R, Kamat K, Inamdar MS. The OCIAD protein family: comparative developmental biology and stem cell application. *Int J Dev Biol.* 2020. <https://doi.org/10.1387/ijdb.190038mi>.
65. Ray A, Kamat K, Inamdar MS. A conserved role for Asrij/OCIAD1 in progenitor differentiation and lineage specification through functional interaction with the regulators of mitochondrial dynamics. *Front Cell Dev Biol.* 2021;6(9):643444.
66. Deczkowska A, Keren-Shaul H, Weiner A, Colonna M, Schwartz M, Amit I. Disease-associated microglia: a universal immune sensor of neurodegeneration. *Cell.* 2018;173(5):1073–81.
67. Gao C, Jiang J, Tan Y, Chen S. Microglia in neurodegenerative diseases: mechanism and potential therapeutic targets. *Sig Transduct Target Ther.* 2023;8(1):359.
68. Jay TR, Miller CM, Cheng PJ, Graham LC, Bemiller S, Broihier ML, et al. TREM2 deficiency eliminates TREM2+ inflammatory macrophages and ameliorates pathology in Alzheimer's disease mouse models. *J Exp Med.* 2015;212(3):287–95.
69. Samuels JD, Moore KA, Ennerfelt HE, Johnson AM, Walsh AE, Price RJ, et al. The Alzheimer's disease risk factor *INPP5D* restricts neuroprotective microglial responses in amyloid beta-mediated pathology. *Alzheimer Dement.* 2023;19(11):4908–21.

Publisher's Note

Springer Nature remains neutral with regard to jurisdictional claims in published maps and institutional affiliations.